CLUSTERING–BASED TIME RESOLVED SPECTRAL INVESTIGATIONS OF BURSTS FROM MAGNETAR SGR J1550−5418

by
MUSTAFA DEMİRER

Submitted to the Graduate School of Engineering and Natural Sciences
in partial fulfillment of the requirements for the degree of
Master of Science

Sabancı University
December 2023

ABSTRACT

CLUSTERING–BASED TIME RESOLVED SPECTRAL INVESTIGATIONS OF BURSTS FROM MAGNETAR SGR J1550−5418

MUSTAFA DEMIRER

PHYSICS M.SC. THESIS, DECEMBER 2023

Thesis Supervisor: Prof. Dr. ERSİN GÖĞÜŞ

Thesis Co-Supervisor: Dr. YUKI KANEKO

Keywords: neutron star, magnetar, X-ray burst, machine learning

Magnetars, strongly magnetized neutron stars, are the sources of short duration but extremely energetic hard X-ray bursts. This thesis presents a time-resolved spectral analysis of 42 bursts originated from SGR J1550−5418. Our study introduces an innovative approach to time-resolved spectral analysis: Initially, we created overlapping time segments and fitted them using three models: a comptonized model, a double blackbody model, and a modified blackbody model with resonance cyclotron scattering. Subsequently, we tested four distinct algorithms for clustering overlapping time segments, namely; K-means clustering, DBSCAN, agglomerative clustering, and Gaussian mixture. The K-means algorithm was ultimately selected for its effectiveness. After that, we created non-overlapping time segments by fitting the clustered time segments. We employed the Bayesian Information Criterion (BIC) for model comparison. As a result, we found that the COMPT model is most favorable for the most fits, with approximately half of the time segments also being favored by the other two models. Additionally, we observed a deviation from Stefan-Boltzmann trend in kT vs R^2 plot of the double blackbody model. The most notable aspects of this study are that it is the first extensive application of the MBB−RCS model and our novel method combining overlapping time segments with clustering analysis.

ÖZET

MAGNETAR SGR J1550−5418 PATLAMALARININ KÜMELENME BAZLI ZAMAN ÇÖZÜNÜRLÜKLÜ TAYFSAL İNCELEMELERİ

MUSTAFA DEMIRER

FİZİK YÜKSEK LİSANS TEZİ, ARALIK 2023

Tez Danışmanı: Prof. Dr. ERSİN GÖĞÜŞ

Tez Eş Danışmanı: Dr. YUKI KANEKO

Anahtar Kelimeler: nötron yıldızı, magnetar, X-ışını patlaması, makine öğrenmesi

Magnetarlar çok şiddetli manyetik alanlara sahip nötron yıldızları olup, kısa süreli ancak yüksek enerjili X-ışını patlamaları sergilerler. Bu tez, SGR J1550−5418 kaynağından 42 patlamanın zaman çözümlü tayfsal analizini sunmaktadır. Çalışmamız zaman çözümlemeli tayfsal analize yenilikçi bir yaklaşım getirmektedir: Daha önceki çalışmalardan farklı olarak her bir patlama için başlangıçta örtüşen zaman dilimleri oluşturduk ve bunları üç model kullanarak fit ettik: compton modeli, iki kara cisim modeli ve rezonans siklotron saçılımına sahip modifiye bir kara cisim modeli. Daha sonra k-kümeleme, DBSCAN, toplayıcı kümeleme ve Gauss karışımı algoritmalarını zaman dilimlerimize uygulayarak test ettik. Denediklerimizin arasından basit olması ve etkili sonuç vermesi nedeniyle K-kümelenme algoritması ile devam etmeye karar verdik. Sonrasında bu algoritmayı kullanarak birleştirdiğimiz zaman dilimlerini fit ettik ve örtüşmeyen zaman dilimleri oluşturduk. Model karşılaştırması için ise Bayes Bilgi Kriterini (BIC) kullandık. Sonuç olarak; COMPT modelinin neredeyse tüm zaman dilimleri için en uygun model olduğunu, öte yandan zaman dilimlerinin yaklaşık yarısının diğer iki model tarafından tercih edildiğini tespit ettik. Ek olarak, iki kara cisim modelinin kT vs R^2 grafiğinde Stefan-Boltzmann davranışından bir sapma gözlemledik. Bu çalışmanın dikkate değer yönleri, MBB−RCS modelinin ilk kez kapsamlı uygulaması ve örtüşen zaman dilimlerini kümeleme analiziyle birleştiren yeni yöntem olarak sıralanabilir.

ACKNOWLEDGEMENTS

I would like to express my deepest gratitude to my advisor Prof. Ersin Göğüş for his valuable guidance and support. I am particularly grateful for his patience, understanding, and encouragement during the most challenging phases of my study.

I would also like to express my appreciation to my co-advisor Dr. Yuki Kaneko. I am deeply thankful for dedicating her valuable time and effort to this study.

I would like to thank my teammate Özge Keskin. Her generous helpfulness and friendship were crucial in making this thesis possible.

Last but not least, I owe thanks to my family and friends who always supported me throughout my entire life.

I acknowledge support and funding from the Scientific and Technological Research Council of Turkey (TÜBITAK, grant no: 121F266).

TABLE OF CONTENTS

LIST OF TABLES

LIST OF FIGURES

LIST OF ABBREVIATIONS

AXP: Anomalous X-ray Pulsars

BB+BB: Combination of Two Blackbody Functions

BGO: Bismuth Germanate Scintillation Detector

BIC: Bayesian Information Criterion

COMPT: Power Law Model with An Exponential Cut-Off

C-stat: Castor Statistics

DBSCAN: Density-Based Spatial Clustering of Applications with Noise

DRM: Detector Response Matrices

EoS: Equation of State

Epeak: Peak Energy

GBM: Gamma-ray Burst Monitor

LAT: Large Area Telescope

MBB-RCS: Modified Blackbody with Resonance Cyclotron Scattering

MET: Mission Elapsed Time

NaI(Tl): Thallium Activated Sodium Iodide Scintillation Detector

QPO: Quasi-Periodic Oscillation

SGR: Soft Gamma Repeater

TTE: Time-Tagged Events

XSpec: X-ray Spectral Fitting Package

1. INTRODUCTION

Magnetars represent a small class of isolated neutron stars with extremely strong magnetic fields. Due to enormous stresses by these strong fields, magnetars emit highly energetic bursts. SGR J1550−5418 , is one of the prolific magnetars: It emitted hundreds of bursts during its most active episode in 2009 detected with multiple space-based telescopes including Gamma-ray Burst Monitor (GBM) on board the Fermi Gamma-ray Space Telescope. A sample of brightest bursts from SGR J1550−5418 detected with GBM is the focus of this thesis.

1.1 Neutron Stars

A neutron star is a compact object that forms after a supernova explosion of a massive star. Typically, stars spend most of their lives in a balance between its own gravity and outward radiative pressure. However, as the star approaches the end of its life, namely when the core is iron rich, its fusion power drops and it cannot provide the necessary radiative pressure to support inward force of gravity. At this stage, gravity takes over and the core of the star begins to collapse. In the case of massive stars ($M > 8M_{\odot}$; Woosley et al., 2002), this collapse exerts immense pressure at the star's core. This intense pressure triggers neutronization through inverse beta decay. A neutron star could then form if the newly formed neutron rich central structure achieves stability via degeneracy pressure of neutrons against the infalling mass. The core collapse process could also give rise to the formation of a black hole if the gravitational force of the infalling mass exceeds the opposing neutron degeneracy pressure.

1.1.1 Brief History of Neutron Stars

Baade & Zwicky (1934) coined the term neutron star, shortly after the discovery of neutrons by Chadwick (1932). They proposed that supernova explosions could end in the formation of extremely dense, compact objects predominantly composed of neutrons. However, observational evidence for such type of celestial objects come more than 30 years later. Hewish & Okoye (1965) detected "an unusual source of high radio brightness" in the Crab Nebula. Subsequently, Jocelyn Bell observed periodic oscillations from this same source (Hewish et al., 1968), leading to the discovery of the first observational manifestation of neutron stars.

Following the initial observation of a pulsar, binary systems containing pulsars were also discovered (Hulse & Taylor, 1975). While the first pulsar was detected in radio wavelengths, subsequent discoveries have revealed pulsars emitting across various regions of the electromagnetic spectrum, including optical pulsars (Cocke et al., 1969), X-ray pulsars (Giacconi et al., 1971), and gamma-ray pulsars (Kniffen et al., 1974).

Over more than half a century since their observational discovery, significant progresses have been made in understanding neutron star systems. A notable example is the identification of millisecond pulsars (Backer et al., 1982). These are old neutron star systems with low magnetic fields ($\sim 10^9$ G) in binary systems. They could possess such high frequency rotation rates through the spin-up process via transfer of matter from their companion stars in binary systems (Alpar et al., 1982). On the other extreme, X-ray pulsations and spin-down rate measurements from a soft gamma repeaters (SGRs) yielded an inferred magnetic field strength exceeding 10^{14} G, marked the discovery of magnetars (Kouveliotou et al., 1998). These systems will be investigated in Section 1.2.

1.1.2 Properties of Neutron Stars

A typical neutron star has a radius of ~ 10 km and a mass of ~ 1.4 $M_\odot$. The minimum allowed mass of a neutron star is considered ~ 1.17 $M_\odot$, which can be observed in the mass of the neutron star in a binary system of PSR J0453+1559 (Suwa et al., 2018). Conversely, the maximum allowed mass of a neutron star depends on its equation of state (EoS), which remains uncertain at higher densities at the interior of neutron star (ranging between $2\rho_0$ and $10\rho_0$, where nuclear density

$\rho_0 = 2.8 \times 10^{14}$ g cm^{-3}). However, it is generally assumed to be between 2 $M_\odot$ and 3 $M_\odot$ (Chamel et al., 2013). The most massive neutron star observed to date has a mass of 2.35 ± 0.17 $M_\odot$ (Romani et al., 2022).

It is expected that a newborn neutron star has a very high temperature (of the order of 10^{10} K). Neutron stars rapidly cool via neutrino emission via direct and modified Urca-processes (Gamow & Schoenberg, 1941). If the direct Urca-processes occur, the liquid core would cool to 10^9 K in about a minute and reach 10^8 K roughly within a week. However, the cooling to 10^9 K will be slightly slower due to the neutrino and anti-neutrino absorption in the direct Urca core, extending this time to several tens of minutes (Haensel & Schaeffer, 1992). On the other hand, if the non-direct Urca-processes occurs, the core's cooling to 10^9 K would take approximately a year, and reaching 10^8 K would require around 10^6 years (Haensel, 1995).

The magnetic fields of neutron stars vary from 10^8 G (old systems) up to 10^{15} G (magnetars). At birth, magnetic fields are believed to originate from the conservation of magnetic flux during the dramatic shrinkage of radius of the progenitor star to the much smaller radius of the neutron star (e.g. from R $\sim 10^{11}$ cm to R $\sim 10^6$ cm; see Igoshev et al., 2021, for details). Additionally, various dynamo could amplify the magnetic fields of new born neutron stars (Lander, 2021).

1.2 Magnetars

Magnetars are a subcategory of neutron stars that share similar characteristics with typical neutron stars. However, they are distinguished from neutron stars in terms of their enormous magnetic fields ($\gtrsim 10^{14}$ G, Duncan & Thompson, 1992). This intense magnetic field of magnetars leads to a wide range of emission features primarily in X-rays and gamma rays. The most distinctive magnetar activity is the repeated emission of short duration but highly energetic bursts in hard X-rays. These events were actually discovered with the Venera 11 & 12 spacecrafts in the late 1970s (Mazets et al., 1979). They observed an initial narrow spike of about ~ 15 ms and a longer tail of about ~ 150 ms. After observing recurring bursts from the same source, a new class of burst sources were introduced: Soft Gamma Repeaters (SGRs) and the first such source being SGR J1806−20 (Atteia et al., 1987; Laros et al., 1987).

Along with SGRs, another small class of bright X-ray sources have been exhibiting intriguing persistent X-ray emission properties (Gregory & Fahlman, 1980). Based

on their relatively long pulse periods and atypical X-ray spectra, they were called Anomalous X-ray Pulsars (AXPs; van Paradijs, Taam & van den Heuvel, 1995). The surface magnetic field strengths inferred from their spin period and spin-down rates were already indicating that they could possess extremely strong magnetic fields. Observations of SGR-like burst from AXPs (Gavriil, Kaspi & Woods, 2002) united these two groups, which collectively form the family of magnetars. To date, there are nearly 30 confirmed magnetars (Olausen & Kaspi, 2014).

Transient radiative behaviour of magnetars can be studied under three primary classifications: Typical bursts, Outbursts, Giant Flares. Magnetar bursts are short events, lasting from a few milliseconds to seconds, with a peak of distribution around 100 ms (Kaspi & Beloborodov, 2017). Peak luminosities of these bursts vary from 10^{38} to 10^{43} erg s^{-1}. Bursts are commonly single-peaked with a fast rise and a slower decay, while there have been observations of bursts with multiple peaks (Göğüş et al., 2001). Occasionally, bursts with emission tail that can last several minutes are observed. (see; e.g. Göğüş et al., 2011; Muş et al., 2015).

Outbursts are sudden increases in the persistent X-ray flux of magnetars. The flux elevation at the onset of an outburst can be as high as a 1000 fold, reaching the level of 10^{36} erg s^{-1} (see Rea & Esposito, 2011, for a review). For most outbursts, there are typically associated timing anomalies, usually a glitch or an anti-glitch, which is a sudden spin-up or spin-down of a pulsar (Kaspi & Beloborodov, 2017). The flux of the outburst initially decays quite fast, occurring within a few minutes to hours. Subsequently, the rate of decay slows down, stretching over several months or even years (see e.g. Woods et al., 2004). Some magnetars do not show an outburst for many years (e.g. 1RXS J1708-4009; Dib & Kaspi, 2014), in contrast, some can have multiple outbursts (e.g. SGR 1806-20; Göğüş et al., 2011).

Giant Flares are the brightest bursts originating from magnetars. To date, only three such giant flares have been recorded. From SGR 0526-66 on March 5, 1979 (Evans et al., 1980), from SGR 1900+14 on August 27, 1998 (Hurley et al., 1999), and from SGR 1806-20 on December 27, 2004 (Hurley et al., 2005). These events reached peak X-ray luminosities within the range of 10^{44} to 10^{47} erg s^{-1}, and a total energy release exceeding 10^{44} erg in the hard X-rays and gamma-ray band. Particularly, the December 27, 2004 event was at least 100 times more energetic than the other two, even outshining all stars in our galaxy 1000 times.

1.2.1 SGR J1550−5418

SGR J1550−5418, the source of bursts studied in this thesis, was first observed with the Einstein X-ray satellite and was originally designated with the name, 1E 1547.0−5408 (Lamb & Markert, 1981). Its monitoring with the Parkes Radio Telescope led to the discovery of its spin period $P = 2.069$ s and the spin-down rate of $\dot{P} = 2.3 \times 10^{-11}$ (Camilo et al., 2007). Therefore, the inferred magnetic dipole field strength of 2.2×10^{14} G made this system the first magnetar identified via radio observations.

After a long silence in X-rays, SGR J1550−5418 became active again in 2008 when its three episodes of burst activity started. The first of these episodes began in October 2008, featuring dozens of bursts (von Kienlin et al., 2012). The second episode, starting on January 22, 2009, was the most active phase for the source, emitting hundreds of bursts (van der Horst et al., 2012). The third significant burst activity for SGR J1550−5418 occurred between March and April 2009. In this thesis, mainly the bursts that took place in the second episode were analyzed.

Extensive investigations have been conducted to examine the spectral characteristics of short bursts from various magnetars, employing both thermal and non-thermal models (see e.g., Collazzi et al., 2015; Feroci et al., 2004; Israel et al., 2008). Specifically for the bursts from SGR J1550−5418 , Lin et al. (2012), van der Horst et al. (2012), and Kırmızıbayrak et al. (2017) have performed thorough time-integrated spectral analyses. These comprehensive investigations have shown that the spectra can be effectively described either by a combination of two blackbody functions (BB+BB) or by a power law model with an exponential cut-off (COMPT).

Younes et al. (2014) conducted an in-depth time-resolved spectral analysis of a set of bright bursts from SGR J1550−5418, aiming to overcome the limitation of time-integrated analyses where the brightest moments dominate the overall picture. This approach intended to provide a more clearer understanding of the bursts' dynamics and spectral characteristics, using BB+BB and COMPT models. In the COMPT model fits, they observed a negative correlation between flux and the peak energy ($E_{\rm peak}$) up to a flux limit of approximately $F \approx 10^{-5}$ erg s^{-1} cm^{-2}, after which the correlation turns positive. Meanwhile, the BB+BB model fits indicated that the relationship between the emission region's area and temperature follows a broken power law with a generally negative trend. For lower flux bursts, this trend remains consistent with a single power law across temperatures, but a break in the power law emerges at higher flux levels, possibly due to adiabatic cooling (Younes et al., 2014). However, the spectral data were extracted from arbitrarily selected time intervals,

with each successive spectrum accumulated until reaching a certain signal-to-noise ratio. This arbitrary selection might obscure the true spectral evolution within the bursts, thereby limiting a deeper understanding of the spectral properties of magnetars.

In this thesis, we introduce a new approach to the time-resolved spectral analysis of 42 bright Fermi GBM detected bursts from SGR J1550−5418, distinguished by our unique method of creating time segments, which differs significantly from previous analysis methods. Unlike earlier studies that formed time segments uniformly or based on signal-to-noise ratios, our approach involves generating overlapping time segments as a preliminary step. Then, to accurately identify the points of spectral change within the bursts, we utilized machine learning-based clustering algorithms. These algorithms were applied to create time segments of varied lengths, determined by the spectral parameters derived from the initial phase. This innovative approach has enabled us to achieve a more profound understanding of the burst data being examined.

The next section provides a brief description of Fermi GBM detectors, its data types, and in depth description of our methodology for the innovative time-resolved spectral investigations including a machine learning-based spectral clustering application. We present our results in Section 3, and discuss their implications in Section 4.

2. METHOD

2.1 The Fermi Gamma-ray Space Telescope

The Fermi Gamma-ray Space Telescope, designed for observing transient events in the gamma-ray sky, was launched on June 11, 2008, into a 565 km orbit. Aboard the telescope are two primary scientific instruments: the Large Area Telescope (LAT) and the Gamma-ray Burst Monitor (GBM). The LAT can detect gamma-ray bursts with energies exceeding ~ 20 MeV. The GBM detectors were developed to observe objects in the lower energy band, ranging from ~ 8 keV to ~ 40 MeV (Meegan et al., 2009).

2.1.1 GBM Detectors

The GBM includes two types of detectors: 12 thallium activated sodium iodide (NaI(Tl)) scintillation detectors, and two bismuth germanate (BGO) scintillation detectors. The NaI(Tl) detectors provide a lower energy spectrum, from ~ 8 keV to ~ 1 MeV, and can encompass the entire sky through the diverse orientations of the 12 detectors. On the other hand, BGO detectors provide an intermediate energy spectrum between NaI(Tl) detectors and the LAT, with a range of ~ 200 keV to ~ 40 MeV. Positioned on opposite sides of the spacecraft, the two BGO detectors ensure that any event above the horizon can be detected by at least one of these detectors. Furthermore, the BGO detectors' intermediate position in the energy spectrum, between NaI(Tl) and LAT, allows them to serve as a calibration tool for the other detectors (Meegan et al., 2009).

2.1.2 Data Types

The Fermi/GBM produces three types of data: CTIME, CSPEC, and TTE. CTIME offers a finer time resolution (256 ms) but coarser spectral resolution (8 channels), while CSPEC, in contrast, provides the opposite with a coarser time resolution (4096 ms) and finer spectral resolution (128 channels). However, upon detector triggering, these time resolutions significantly improve: CTIME to 64 ms and CSPEC to 1024 ms. They revert back to the sky monitoring resolution 600 seconds after the trigger event. Additionally, the third data type, known as "time-tagged events" (TTE), is recorded along with each event's arrival time (with precision of 2 μs) and energy (including 128 channels). The TTE data is continuously stored in a buffer and telemetered periodically. When the GBM triggers, buffered data along with 300 seconds of post-trigger TTE data is transmitted (Gruber et al., 2014).

In our project, we utilized the TTE data from the Fermi/GBM detector due to its superior resolution both in time and energy compared to the other two data types. Given that the observed energy range of the SGRs are lower than ~ 200 keV (Lin et al., 2012; van der Horst et al., 2012; Younes et al., 2014) we employed the NaI(Tl) detectors of the GBM.

2.2 Data Selection and Preparation

We used a large sample comprising 386 bursts from the 2008-2009 active episode of SGR J1550−5418 , compiled from the burst catalog presented in Collazzi et al. (2015). From this sample, we selected 74 bursts using a criterion of a minimum of 1200 background-subtracted counts in the brightest detector (the detector with the smallest zenith-to-source angle, explained below), aiming to include only those bursts with statistically significant data. 30 bursts among our selection are saturated, meaning that some portion of their data exceeded the readout capability of GBM system (that is, 375000 counts/s with all 14 detectors). Consequently, we proceeded by excluding these saturated portions from these bursts in our analysis. We conducted our study within the 8 to 200 keV energy spectrum, utilizing a minimum time resolution of 4 ms.

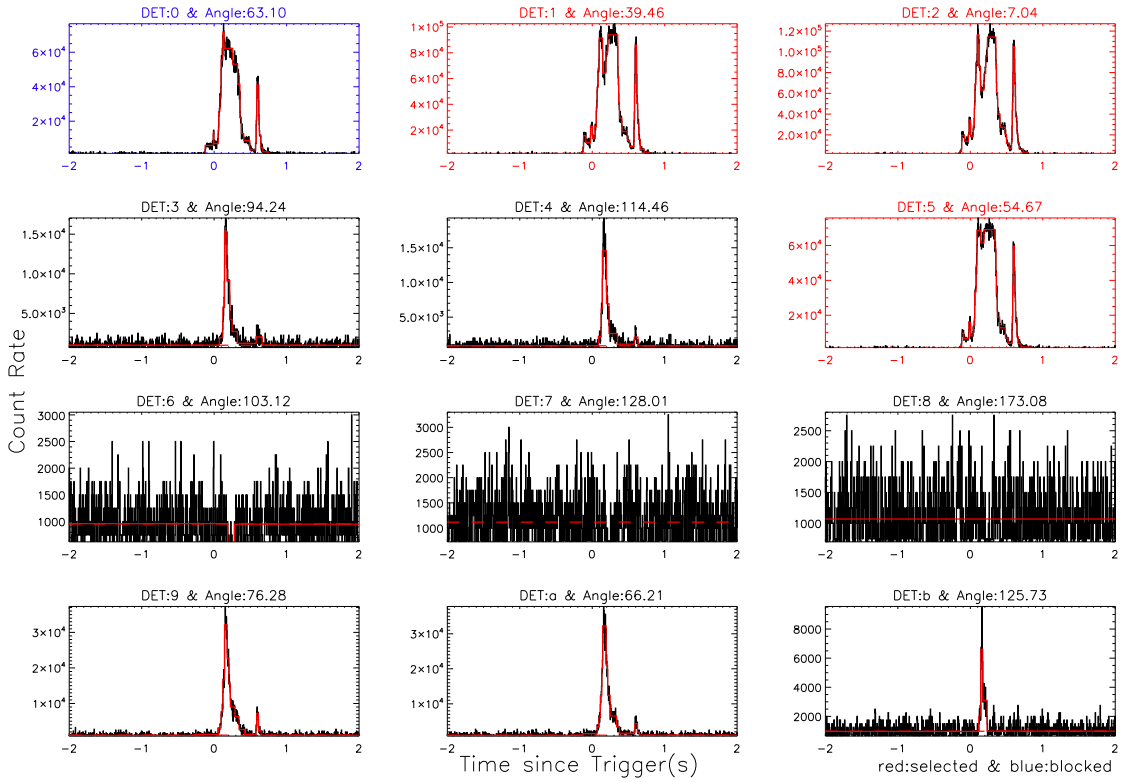

Figure 2.1 Light curves for 12 NaI(Tl) detectors of the burst occurred at 254299790.321 MET (Mission Elapsed Time, the time in seconds since midnight of January 1, 2001). The plots framed with red indicate the detectors chosen for analysis. The blue-framed plot shows the blocked detector. Red blocks on top of each light curve are Bayesian block representations of light curves.

2.2.1 Detector Angle Threshold

Due to the placement of Fermi/GBM NaI(Tl) detectors on the spacecraft, multiple detectors can simultaneously observe the same event. However, the signal-to-noise ratio diminishes as the detector zenith-to-source angle increases. See Figure 2.1 for the light curves of a burst obtained with the data collected with all 12 NaI detectors. Thus, it is essential to extract data only from detectors where the angle does not exceed a certain threshold. In this regard, we tested 45 degrees and 60 degrees as potential threshold angles. We selected 10 bursts which include 2 detectors with 45 degree limit and 3 detectors with 60 degree limit to see the difference in spectral analysis results. We subjected both to tests in XSpec[1] with a single blackbody model. As it can be seen in Figure 2.2 fit parameter kT results with a 60-degree

[1]XSpec is an x-ray spectral analysis tool specifically designed for astrophysical studies (Arnaud, 1996).

threshold are more constrained since an increase in data points creates better statistics. We set a 60-degree threshold and consequently, for many bursts, we utilized data from 3 detectors, while in some cases, only 2 detectors were used. Moreover, from our analysis, we eliminated detectors that were partially or entirely obstructed by the spacecraft, as determined using the GBMBLOCK software provided by the GBM team.

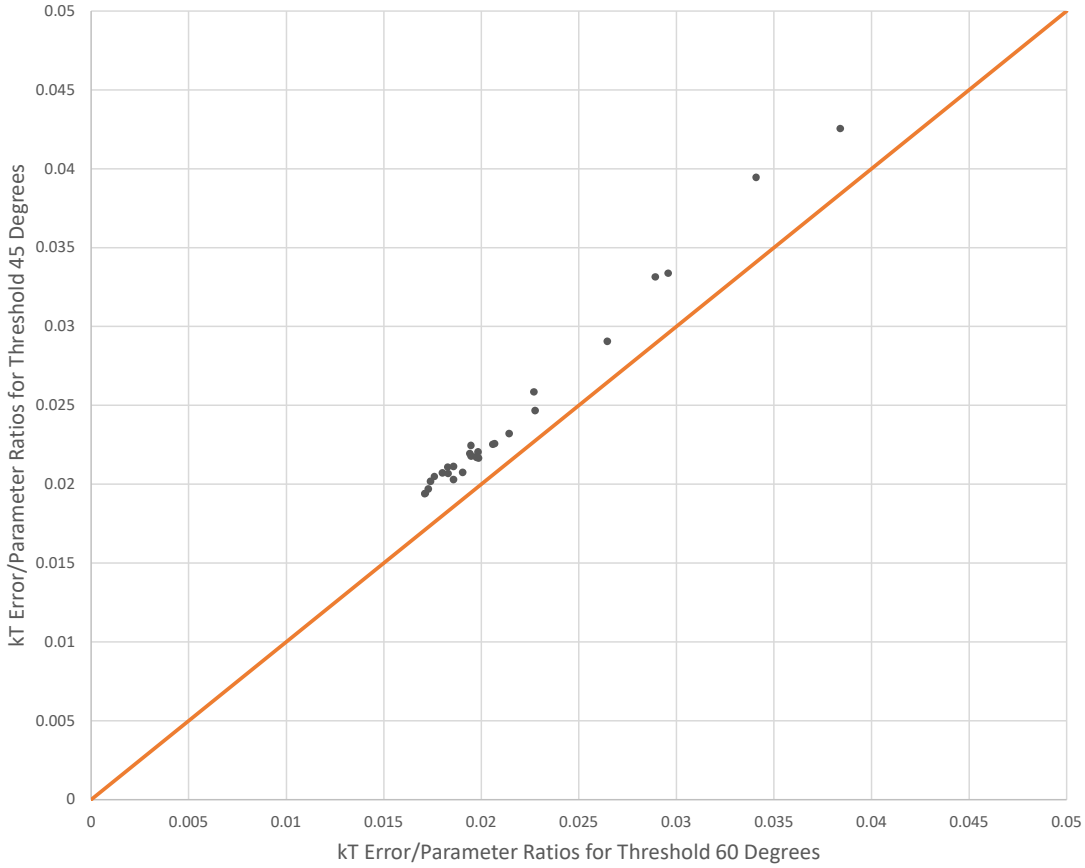

Figure 2.2 Ratios of kT errors/kT with detectors less than 60 degrees vs. 45 degrees included in single BB fit. The solid line indicates a 1-1 relation.

2.2.2 Burst Interval (Duration) Determination

We determined burst durations using a Bayesian approach in order to accurately identify burst intervals, within which burst spectra are to be extracted. For this purpose, we used data collected from the brightest NaI(Tl) detector from Fermi/GBM. For each burst, we first constructed a light curve with a 4 ms time resolution for the time window from –10 seconds to +10 seconds taking the burst trigger time listed

in Collazzi et al. (2015). We then generated Bayesian blocks (Scargle et al. 2013) from this light curve. Blocks with a duration longer than 4 seconds were classified as background, and background level was calculated by taking the average count rates of these blocks. The blocks that were shorter than 4 seconds and higher than the background level around the trigger time were identified as bursts. The burst interval (duration) was then determined as the interval from the start of the first burst block till the end of the last burst block (see Table 2.2 for burst durations).

2.2.3 Overlapping Time Segment Creation

Before generating overlapping time segments, we first produced background-subtracted light curves. We selected the nominal background level by averaging the rates in the time interval between –50 and –1 s before the burst start time as obtained with the Bayesian blocks technique. We then generated background-subtracted light curve with a 4 ms time resolution.

Our goal is to analyze each burst by breaking it down into the maximum number of time segments, while also ensuring that these segments have enough burst counts to conduct a statistically acceptable spectral analysis. Therefore, we needed to determine the appropriate threshold for background-subtracted counts of each time segment. Hence, we conducted spectral analyses on a sample of bursts using six threshold count values: 600, 1000, 1200, 1500, 1800, and 2000 counts. We extracted time-resolved spectra with each of these threshold counts and we fitted them with the three mostly favored continuum models: a blackbody, the sum of two blackbody functions, and a power law with an exponential cutoff (these models are further explained in detail in Section 2.3.1). For each spectrum fitted with each of the three models, we calculated the ratio of best-fit model parameter error to the corresponding parameter value and determined the percentage of ratios that exceed 50%, which indicates not well-constrained fit results. In Table 2.1, we present the collective performances of these models for given count thresholds in determining their model parameters. As a result, we concluded that all model parameters can reasonably be constrained with a minimum of 1200 burst counts.

Table 2.1 Table of time segments percentages of the burst 254297017.989 MET that ratio of fit parameter error/fit parameter exceed 50% threshold with various photon counts.

Number of Time Segments	29	23	19	16	13	13
Photon Count	600	1000	1200	1500	1800	2000
kT (Single Blackbody)	0%	0%	0%	0%	0%	0%
kT_l (Sum of Two Blackbodies)	0%	0%	0%	0%	0%	0%
kT_h (Sum of Two Blackbodies)	10%	4%	0%	0%	0%	0%
Γ (Power Law with an Exp. Cutoff)	0%	0%	0%	0%	0%	0%
E_{peak} (Power Law with an Exp. Cutoff)	0%	0%	0%	0%	0%	0%

Subsequently, we created time segments that were 80% overlapping in time, each containing at least 1200 background-subtracted counts (see Figure 2.3). However, during the burst peak, these overlapping segments tended to accumulate and more than two time intervals overlap at the same time. To overcome this issue, we iteratively reduced the overlap by 5% per iteration until the end of each subsequent time segment occurred later than the end of the previous one.

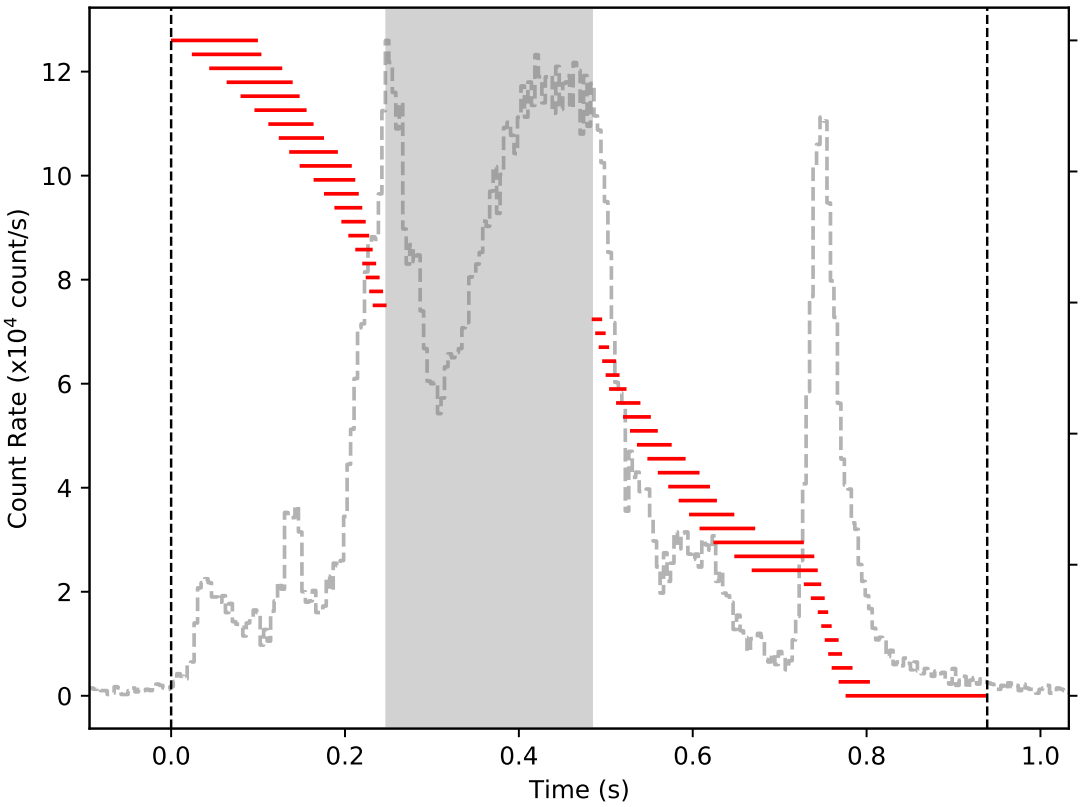

Figure 2.3 Light curve of the burst detected at 2009 January 22 06:49:48.321 UTC (254299790.321 MET) as seen with the brightest detector (n2). Black vertical dashed lines show Bayesian block duration start and end times. Red horizontal bars represent the 48 overlapping time segments with each subsequent segment having an overlap of 80% in time. The gap in the middle (shaded range corresponds to the saturated part of the burst excluded from the analysis.

2.3 Spectral Analysis Methods

In our time-resolved spectral analysis, we implemented a novel approach for time binning that deviates from conventional methods, which typically rely on the observed signal strength to determine the length of time segments. Our method comprises two stages: First, we created overlapping time segments as explained in the previous section, and then fitted these time segments with our photon models described below. After that, we employed the K-means clustering method to cluster the overlapping time segments, using the spectral parameters obtained from the fit results as the basis for clustering. We determined non-overlapping time segments using these clusters. In the final step, we fitted these non-overlapping segments again with the

same photon models to obtain our results.

2.3.1 Continuum Photon Models

We utilized three different spectral models in our study, namely, a power law with an exponential cut-off (COMPT), the sum of two blackbodies (BB+BB), and a modified blackbody with resonance cyclotron scattering (MBB-RCS; Lyubarsky, 2002; Yamasaki et al., 2020), each of which is described below.

2.3.1.1 Power Law with an Exponential Cut-Off (COMPT)

This model is conventionally defined in XSpec as:

$$A(E) = KE^{-\alpha}\exp[-E/E_o] \tag{2.1}$$

where K is the photon flux measured at the pivot energy of 1 keV, Γ is the photon index and E_0 is the E-folding energy. This model mimics the spectral shape of Comptonized burst photons emerging from the trapped fireball (burst sites) near the surface of a magnetar. However, we implement a more intuitive parametrization of this function as:

$$A(E) = K(E/50\text{ keV})^{\Gamma}\exp\left[-E(2+\Gamma)/E_{\rm peak}\right] \tag{2.2}$$

where we change the pivot energy as 50 keV to optimize for the spectra of magnetar bursts. Here $E_{\rm peak}$ corresponds to the energy at which $E^2A(E)$ function peaks, and the two characteristic energies $E_{\rm peak}$ and E_0 are related as follows:

$$E_{\rm peak} = (2+\Gamma)E_0 \tag{2.3}$$

2.3.1.2 Sum of Two Blackbodies (BB+BB)

This model is the summation of two blackbody functions (Planck's Law), we utilized the built-in function of XSpec. Below is the equation for a single blackbody:

$$A(E) = \frac{K \times 8.0525 E^2 \mathrm{d}E}{(kT)^4 \left(\exp\left(\frac{E}{kT}\right) - 1\right)} \tag{2.4}$$

In this equation, k is the Boltzmann constant, T is the temperature, and K is the flux-related normalization parameter. In this way of definition, it is the measure of source luminosity in units of 10^{39} erg/s if the emitting source is at a distance of 10 kpc.

2.3.1.3 Modified Blackbody with Resonance Cyclotron Scattering (MBB−RCS)

Modified Blackbody with Resonance Cyclotron Scattering (MBB−RCS; Yamasaki et al., 2020) is a model that incorporates two physical processes taking place in the vicinity of magnetars, namely the effects of strong magnetic field on the emerging radiation and the effects of resonant cyclotron scattering. The first component (MBB) was suggested by Lyubarsky (2002), who demonstrated using radiative transfer treatments that the emission spectrum following a Planck distribution is altered in the presence of strong magnetic fields. The resulting flux of the emission is expected as follows:

$$A(E) = 0.47 E^2 \left\{ \exp\left[\frac{E^2}{T_{\mathrm{m}} \sqrt{E^2 + (3\pi^2/5) T_{\mathrm{m}}^2}} \right] - 1 \right\}^{-1} \tag{2.5}$$

Here E and T_{m} denote the photon energy and the bolometric temperature respectively. The factor of 0.47 in the equation ensures that total energy flux is preserved. Yamasaki et al. (2020) included the effect resonant cyclotron scattering to the Lyubarsky (2002) model. In this case, photons emitted from a trapped fireball near the surface of a magnetar undergo interactions with magnetospheric electrons or positrons further changing the emerging photon spectrum. To implement

MBB−RCS into XSpec, a table model was generated over the energy range from 5 to 300 keV, consisting of a grid of effective temperatures (T_m) ranging from 1 to 40 keV with energy steps of 0.5 keV.

2.3.2 Spectroscopy and Model Comparison

In our study, we employed the X-ray Spectral Fitting Package (XSpec; version 12.12.1) to conduct spectral analyses. Prior to the analysis, we generated Detector Response Matrices (DRM) for every detector involved in all the untriggered events in our sample. This was achieved using the GBM Response Generator, a tool provided by the *Fermi*-GBM team. We analyzed 509 time segments from 42 bursts.

We employed three different models for fitting namely; COMPT, BB+BB, and MBB-RCS as explained in the previous section. To quantify our fits statistic, we used Castor statistics (C-stat; Cash, 1979). Since the C-stat is based on likelihood and does not provide a measure for the goodness of fit. For this reason, we employed the Bayesian Information Criterion (BIC; Liddle, 2007) as our metric for model preference:

$$\mathrm{BIC} = -2\ln\mathcal{L}_{\max} + m\ln N = \text{C-stat} + m\ln N.$$

Here, $\mathcal{L}_{\max}$ is the maximum likelihood, m represents the number of parameters in the photon model, and N describes the number of data points. To compare models, we evaluated the BIC difference (ΔBIC) between pairs of models (BB+BB vs. COMPT, COMPT vs. MBB−RCS, and BB+BB vs. MBB−RCS), if the difference exceeds 10 (corresponding to a Bayes factor $> \sim$150), we chose the model with lower BIC as the preferred model (Kass & Raftery, 1995) for that specific time segment. If the difference is less than 10, then we considered both two models as equally preferred for the spectrum of that segment.

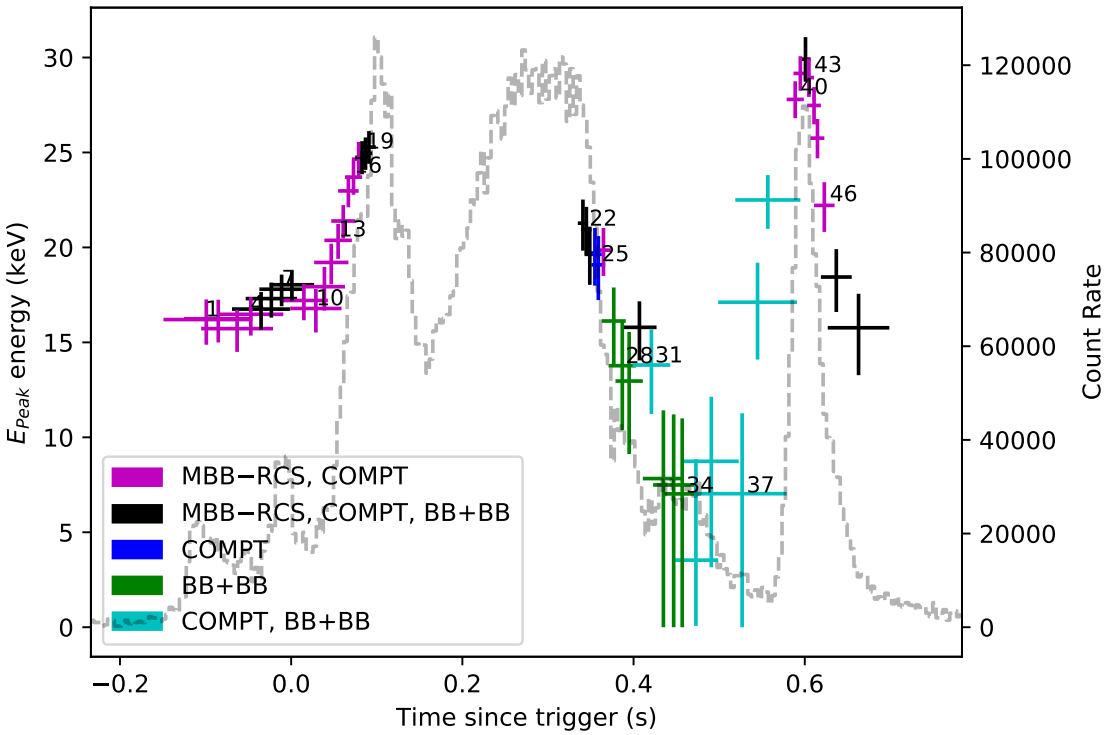

Figure 2.4 values for overlapping time segments for the same burst shown in Figure 2.3. The light curve is shown with grey dashed lines (right axis). The favored models determined by the ΔBIC are shown as color-coded.

After selecting favorable spectral models for each time segment of each burst by comparing BIC values, we obtained the distribution of each fit parameter from favorable fit models (Figures 2.5 and 2.6).

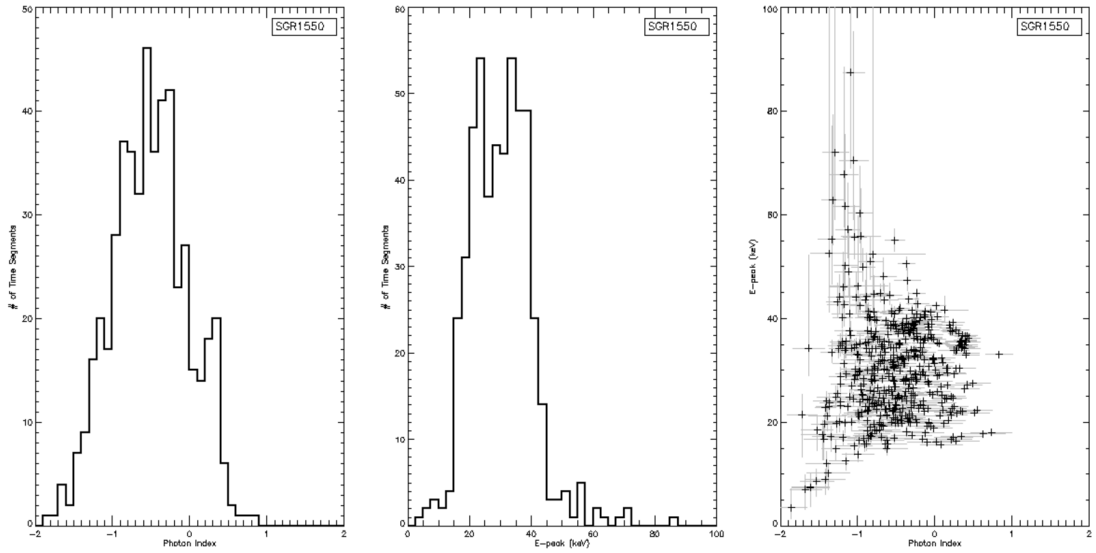

Figure 2.5 Distribution of COMPT parameters: photon index (Γ) and $E_{\rm peak}$ for the first and second graphs respectively. The third graph shows the Γ vs. $E_{\rm peak}$ for each COMPT fit. Here, black plus signs represent the best fit model parameters and grey bars represent the errors with 1σ (corresponds to 68 % confidence level) for each parameter.

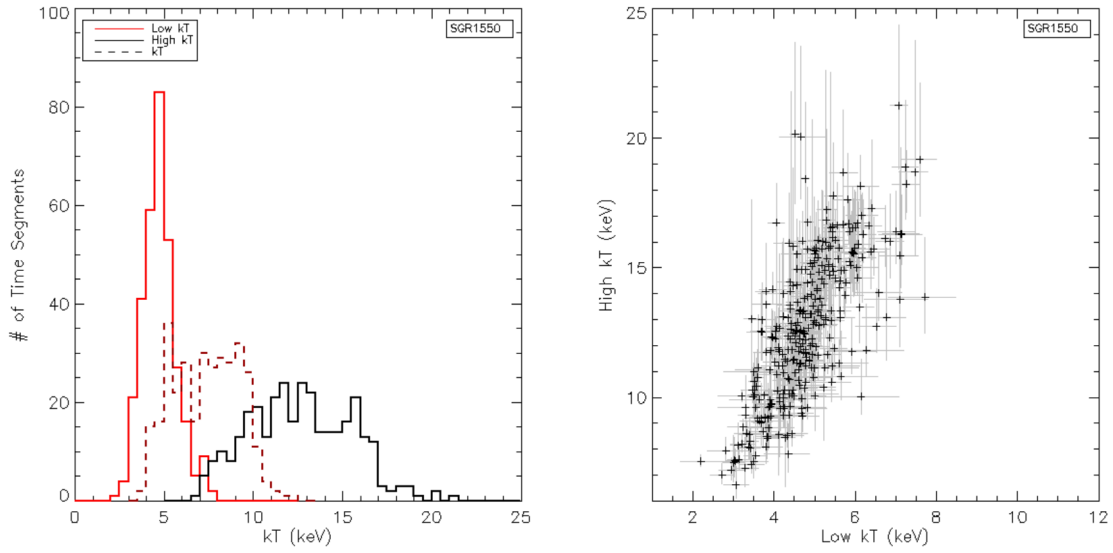

Figure 2.6 [Left] Distribution of thermal model parameters of the overlapping time segmented bursts: Red solid line represents the cooler (low) kT and black solid line shows hotter (high) kT for BB+BB fits. The dashed line presents the kT parameter distribution of the MBB−RCS model. [Right] Cooler kT vs. Hotter kT graph for each BB+BB fit. Grey color represents the model parameter errors with 1σ (corresponds to 68 % confidence level) while black color shows the model parameters.

2.3.3 Clustering Methods

Following the fitting of our three models to the overlapping time segment data, we implemented clustering using different clustering algorithms. This process was conducted using Python programming language (version 3.6.9) and Scikit-learn (version 1.2.1; Pedregosa et al., 2011).

2.3.3.1 *K*-means Clustering

K-means is a common clustering algorithm in data analysis. The main purpose of the algorithm is clustering data points such that the similarity within clusters is maximized and the similarity between different clusters minimized (Lloyd, 1982).

Initially, the algorithm requires the number of clusters, denoted as k. It begins by selecting random samples from the dataset to establish initial centroids (centers of the clusters). The algorithm then proceeds through a two-step iteration: Firstly, it assigns each data sample to its nearest centroid. Secondly, it calculates the mean value of all samples associated with each centroid and defines the mean as the new centroid. This iterative process continues until the squared difference between the previous and current centroids falls below a predefined threshold. Once this threshold is reached, the centroids stabilize, and the clustering process ends.

K-means clustering is one of the simplest and computationally efficient clustering algorithms. Moreover, a weight can be defined for the data point, which is particularly helpful when the data has error bars. However, there are various drawbacks of K-means too. First of all, the algorithm always draws circles (or ellipses due to the scaling). This eliminates the possibility of clusters with different lengths. Furthermore, K-means locate initial clusters randomly, therefore there is always a possibility of converging to a local extremum point instead of the global extremum. Nonetheless, there are some algorithms like running the algorithm multiple times or spreading the initial centroids to reduce this issue.

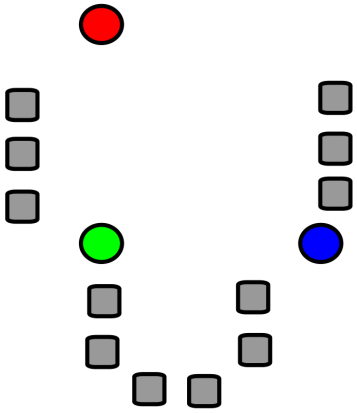

(a) Step 1: Data points shown in gray, random initial centroids shown in red, green and blue.

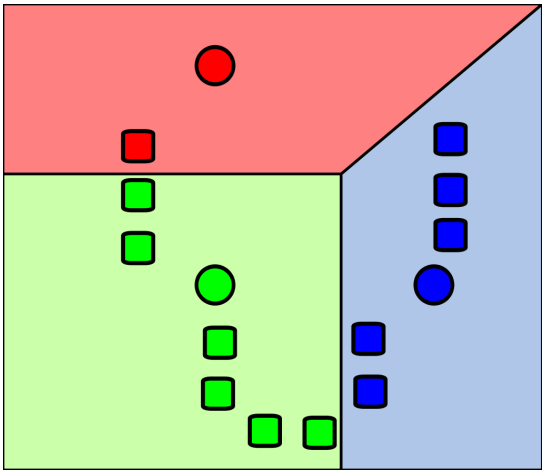

(b) Step 2: Each data point clustered with the color of the nearest centroid.

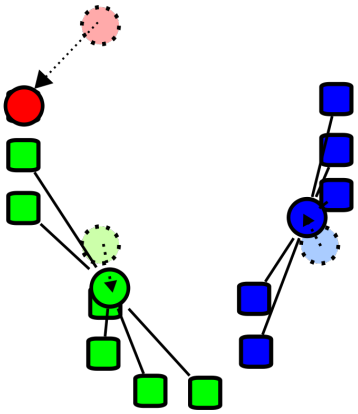

(c) Step 3: Centroids updated according to the mean of the each colored cluster.

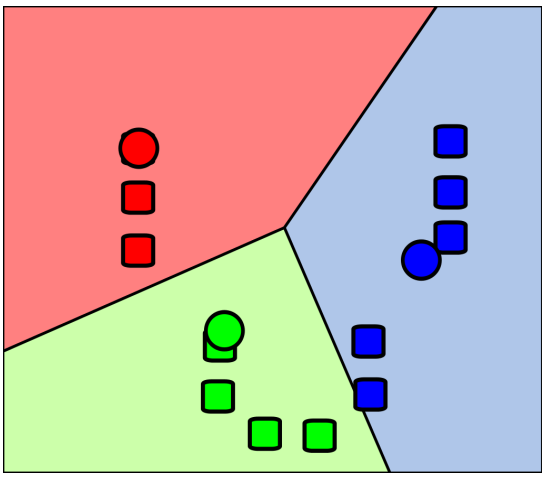

(d) Step 4: Second and third step repeated until the location of centroids are stabilized.

Figure 2.7 Step by step working principle of the K-means algorithm. The figure is taken from Wikimedia Commons, licensed under the CC BY-SA 3.0 license.

2.3.3.2 Density Based Spatial Clustering of Applications with Noise (DBSCAN)

Density Based Spatial Clustering of Applications with Noise (DBSCAN) algorithm is a clustering algorithm based on density (Ester et al., 1996). The algorithm utilizes two main parameters: *eps* and *min_samples*. The *eps* determines how close the

data points should be to form a cluster and, as the name suggests, *min_samples* determines the minimum number of samples to form a cluster. The algorithm begins with drawing circles of *eps* radius around each data point. If there are at least *min_samples* inside the circle, then that data point is defined as a core point. Thus, points inside the circle of a core point are defined as neighbors. All core points that are neighbors of each other and the non-core point neighbors of these core points together form a cluster. In this schema, it is possible for a point to not be a member of any cluster. Such data points are called noise or outliers.

The absence of an initial cluster number parameter is one of the biggest advantages of DBSCAN. In addition, unlike K-means, it does not involve randomness. All steps of the algorithm are deterministic. Therefore it is guaranteed to have the same result in each trial with the same data. Moreover, clusters only depend on density, they do not exhibit a distinct shape. On the other hand, it does not involve a weight parameter. Also, it is not suitable for equal-density data or if all points of the data set should be in a cluster (no noise).

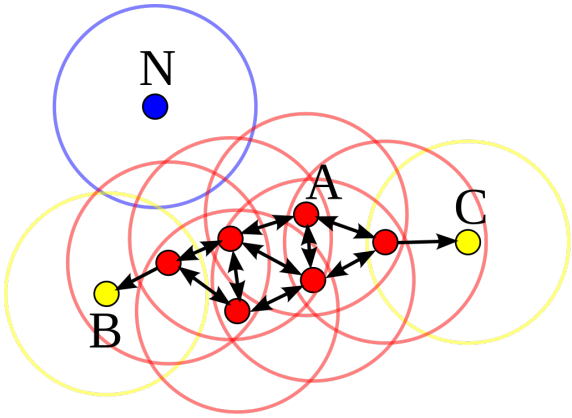

Figure 2.8 DBSCAN clustering algorithm is shown. Red dots are core points, yellow ones are neighbors of core points but themselves are not core points, and the blue one is not connected to any of them, it is considered noise. The figure is taken from Wikimedia Commons, licensed under the CC BY-SA 3.0 license.

2.3.3.3 Agglomerative Clustering

Agglomerative clustering is the "bottom-up" type of hierarchical clustering algorithm. The algorithm starts with defining each data point as a cluster and then merges the points closest to each other according to a metric. It repeats this process step by step until all data points are collected in a single cluster. Hence, a

dendrogram forms from this process. Depending on the parameters, any slice of the dendrogram can be obtained as an ideal clustering of the data set.

The main advantage of agglomeration clustering is the ease of visualizing different numbers of cluster schemas as a dendrogram. Therefore, the most suitable clustering can be determined visually. In addition, it also does not need to specify the number of clusters in the beginning. On the contrary, it is quite computationally expensive and, hence not suitable for big datasets.

2.3.3.4 Gaussian Mixture Model Clustering

Gaussian mixture model clustering assumes that the data points are distributed according to multiple Gaussian distributions with different parameters. Although its principle is similar to K-means, unlike K-means shape of the clusters does not have to be circular (or ellipsoidal), and they can be probabilistic. Gaussian mixture utilizes an expectation maximization method to converge to a group of clusters. In this method, clusters are initially determined via another clustering method or just guessed. Then, each point is assigned a weight due to its probability of belonging to each cluster. After that clusters are updated using the weights. These two steps continue iteratively until a threshold is reached. The major drawback of Gaussian mixture clustering is that it is a complicated algorithm and computationally expensive.

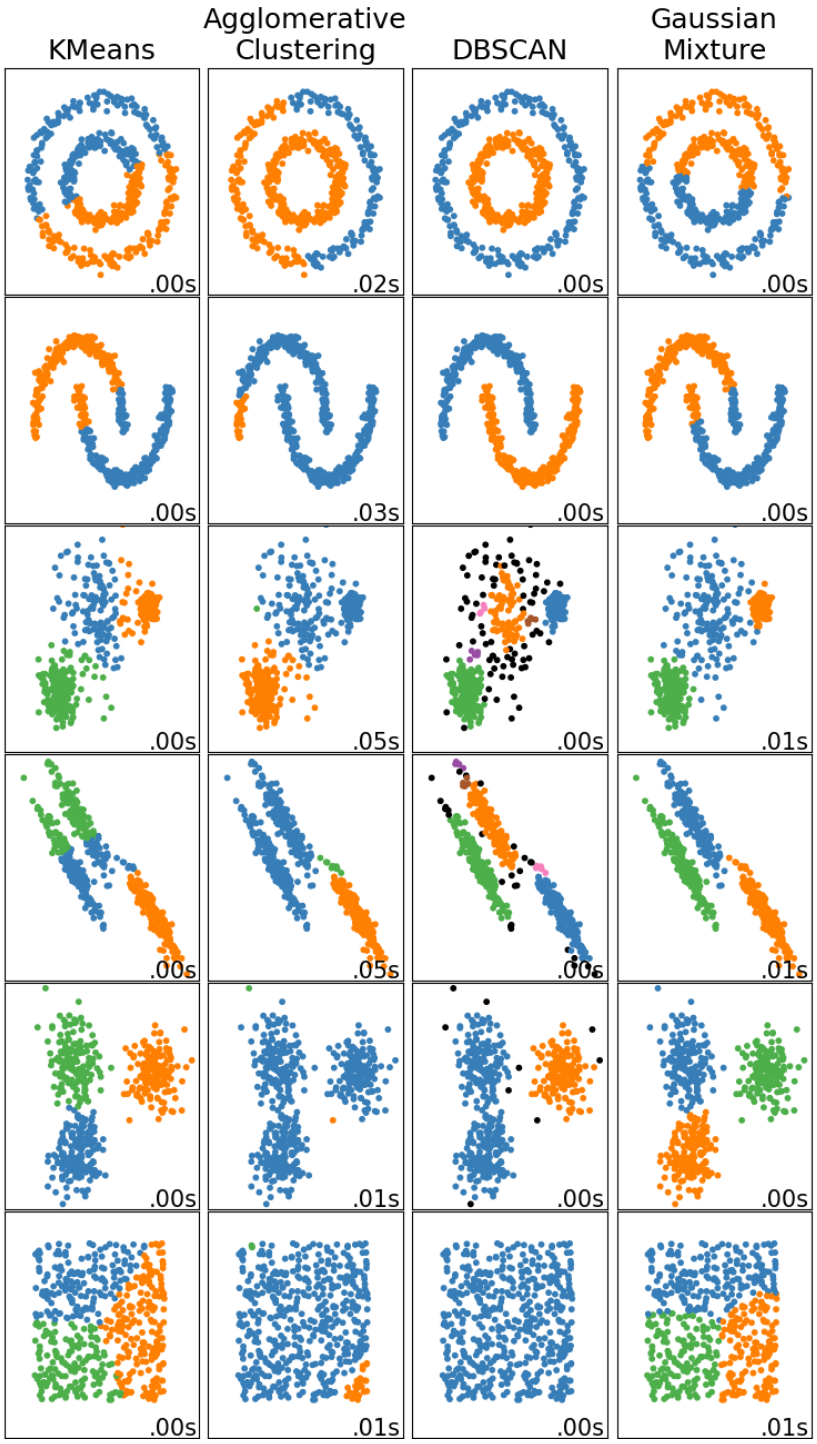

Figure 2.9 Comparison of our four clustering models on various two-dimensional data sets. Different colors in each panel show their resulting clusters. The computation time of each process is shown in the bottom right corner. The figure is taken from Scikit-learn, licensed under the BSD license.

2.3.4 Clustering Implementation

In this work, we investigated the aforementioned four clustering algorithms to cluster the overlapping time segments. We selected the data points subject to clustering as the midpoints of time segments and corresponding $E_{\rm peak}$ values obtained from the COMPT model for each burst. The main reason for selecting $E_{\rm peak}$ as the clustering parameter is that the COMPT model is statistically favorable for nearly all bursts in our sample. Moreover, between Γ and $E_{\rm peak}$ parameters, the latter is more variable throughout the bursts. For the implementation of the algorithms on our data, we began by scaling the data points. This step was crucial for two reasons; (1) the range of $E_{\rm peak}$ and time varies significantly among bursts and (2) in order to prevent one axis from dominating the other one.

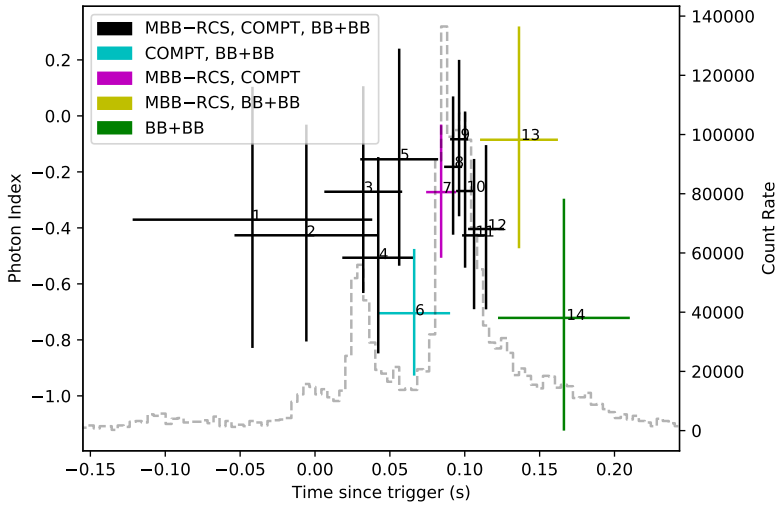

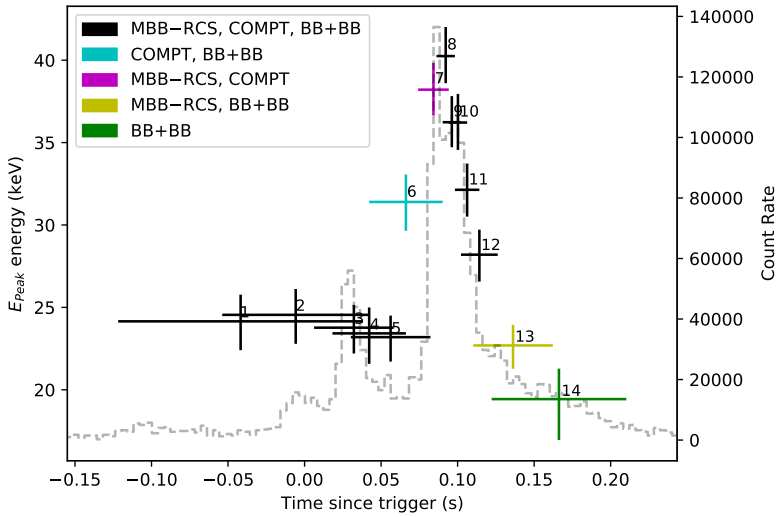

Figure 2.10 Comparison of E_{peak} and Γ parameter variations on a sample burst (MET: 254297017). It can be seen that the E_{peak} parameter varies from around 20 keV to around 40 keV. On the other hand, the range of the Γ parameter is only from about -0.7 to about 0.

After examining all these clustering models described above, we found that DBSCAN does not perform well with equally spaced data, that is time series data. On the other hand, Agglomerative Clustering is suitable but requires extremely long computation time. The Gaussian Mixture and K-means clustering models were found to yield robustness in clustering time segments (that is, discrimination of spectral variations in time). Due to the relative complexity and potential uncertainties involved with the Gaussian Mixture clustering algorithm, we selected to proceed with a simpler and more effective model, which is K-means clustering.

For the implementation of the K-means method, we needed to determine the optimal value for k. To achieve this, we ran the algorithm for all possible k values, ranging from 1 to N–1, where N represents the number of time segments in a particular burst. We then plotted the k values against the inertia, which is the sum of the squared distances of samples to their closest cluster center. The most popular technique to determine k value in such occasions is called the elbow method. By definition, the inertia value of K-means decreases as k increases. However, this decline starts very sharp, and after a point, it decreases more gradually. Hence, the shape of the plot looks like an arm, and the optimal k value is the point where the rate of decrease suddenly changes, so-called the elbow point. However, it is not always possible to have a distinct elbow point in the inertia plot, especially in the bursts with only a few time segments. In such plots, elbow method algorithms fail or do not work properly. Since we have a significant amount of fainter bursts, we saw that the elbow method is failing in such cases.

Therefore, we devised a unique method to identify the optimal point instead of the elbow method. Based on our analyses of sample bursts, we observed that the last 25% of the k values typically fall into this flat region where the inertia does not significantly change. Therefore, we first calculated the average inertia for the top 25% of k values on the inertia graph. Then, we increased this average inertia by adding 1% of the maximum inertia value. The nearest integer to this value was chosen as our optimal k number. We tried this method in some sample bursts and it consistently yielded better results than the heuristic techniques that are commonly used, such as the elbow method. This was particularly evident in bursts with a low number of time segments, where the elbow method often fails to find an elbow point. In contrast, our approach is still effective and applicable.

Lastly, besides k-means clustering, we also experimented with other machine learning clustering techniques such as DBSCAN, agglomerative clustering, and the Gaussian mixture model. As explained in the previous section, we see that DBSCAN is not suitable for our data, and agglomerative clustering, and the Gaussian mixture results were in alignment with those obtained from k-means clustering. However, both two models are much more complicated and computationally expensive when compared to K-means clustering. Therefore, we decided to employ k-means clustering as a reliable method for our analysis.

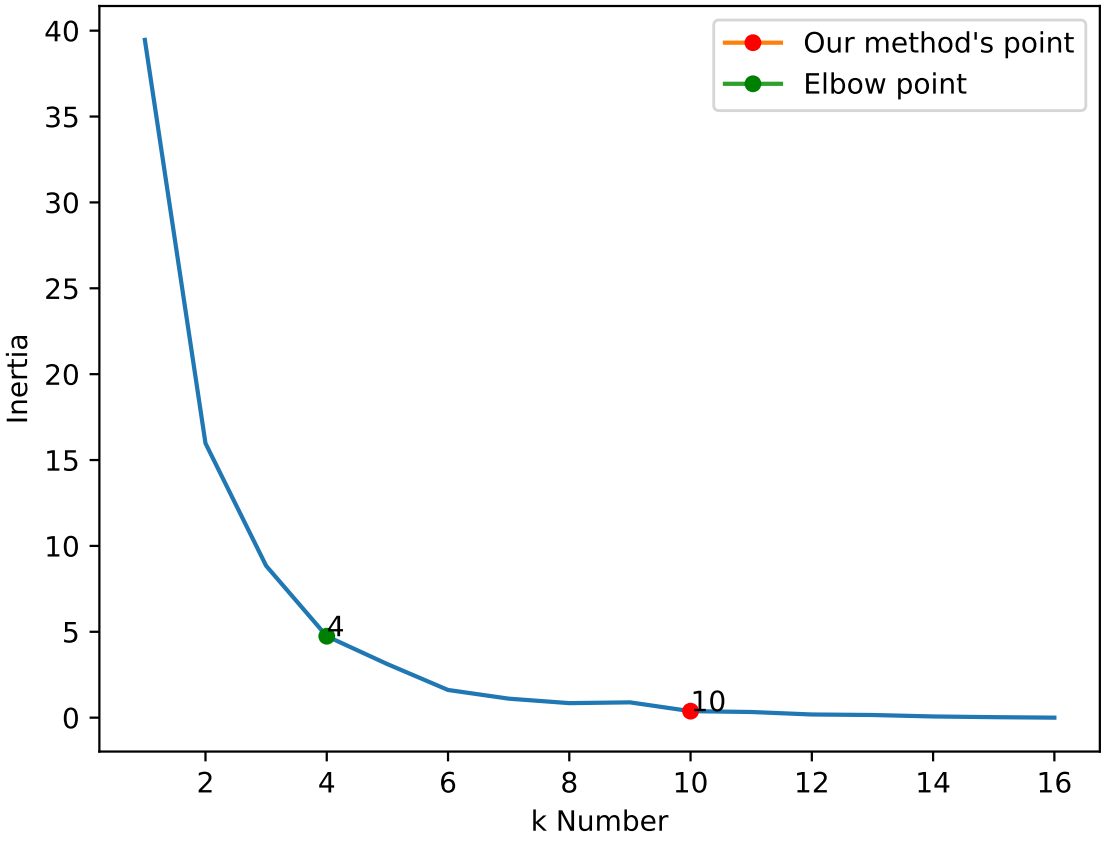

Figure 2.11 Comparison of elbow method and our method in the burst MET: 255384041.494. The x-axis represents different numbers of k, y-axis represents the inertia. As it can be clearly seen, our method gives a more stabilized k value in terms of inertia.

After the clustering process, clusters (groups) of time segments still overlap since each of the time segments was arranged such that it overlaps 80% with the previous time segment. Hence, the last time segment in a cluster overlaps with the first time segment in the adjacent cluster. To be able to create new non-overlapping time segments from these clusters, we removed this overlap by dividing the total background-subtracted counts in the overlapping region in half. Because the number of counts is important to get a meaningful spectral fit result. Therefore, we shared the number of counts in the overlapping region equally between the two clusters. In this way, we finalized the decision of non-overlapping time segments' start and stop points for the extraction of new spectral data. A list of all bursts analyzed in this study is shown in Table 2.2.

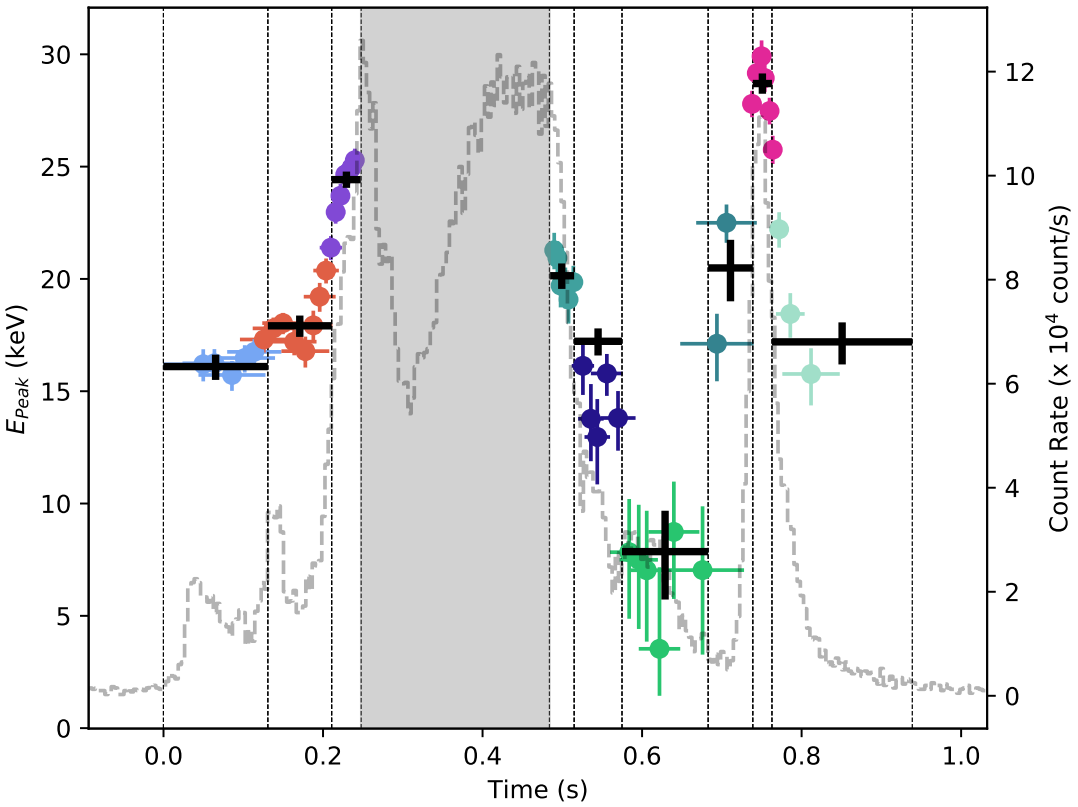

Figure 2.12 $E_{\rm peak}$ values for 48 overlapping time segments (with 1σ uncertainties) for the same burst shown in Figure 2.3. The light curve is shown with grey dashed lines (right axis). The data points were colored by 9 spectrally distinct clusters determined via K-means clustering, the intervals of which are shown with vertical dotted lines. Note that the shaded interval was excluded from the analysis due to count saturation. Black crosses show the $E_{\rm peak}$ values with 1σ uncertainties obtained from the COMPT fits to the nine cluster segments in the second stage of spectral analysis.

Table 2.2 Table of SGR J1550−5418 bursts used in the project.

Burst Date (yymmdd)	**UTC**	**MET**[a] **(s)**	**Duration**[b] **(s)**	**No of Overlapping Time Segments**	**No of Non-overlapping Time Segments**
090122	00:57:20.410	254278642.410	0.656	8	2
090122	01:08:41.706	254279323.706	0.915	11	3
090122	01:14:45.985	254279687.985	0.300	9	2
090122	01:28:59.988	254280541.988	0.516	5	2
090122	01:25:18.640	254280320.640	0.540	6	2
090122	02:32:53.944	254284375.944	0.296	5	2
090122	04:12:33.001	254290355.001	0.849	7	2
090122	04:09:08.677	254290150.677	0.808	8	2
090122	04:34:09.362	254291651.362	0.954	20	6
090122	04:32:49.462	254291571.462	0.687	13	5
090122	05:14:03.372	254294045.372	1.048	12	5
090122	05:16:06.849	254294168.849	0.153	10	3
090122	05:14:29.229	254294071.229	0.891	11	3
090122	06:03:35.989	254297017.989	0.448	15	4
090122	06:49:48.471	254299790.471	0.939	49	9
090122	06:51:14.791	254299876.791	1.165	32	9
090122	06:49:14.841	254299756.841	1.364	27	9
090122	06:49:08.655	254299750.655	0.751	19	4
090122	06:52:03.979	254299925.979	0.678	13	4
090122	06:52:00.167	254299922.167	0.264	7	3
090122	06:50:08.622	254299810.622	0.390	13	3
090122	06:49:32.952	254299774.952	0.548	11	3
090122	06:50:49.339	254299851.339	0.622	4	2
090122	06:49:44.192	254299786.192	0.609	9	2
090122	06:50:12.076	254299814.076	0.419	8	2
090122	06:50:14.271	254299816.271	0.281	7	2
090122	06:59:35.546	254300377.546	1.080	7	2
090122	07:00:58.715	254300460.715	0.665	12	4
090122	07:31:14.748	254302276.748	1.420	22	5
090122	07:40:15.939	254302817.939	0.602	10	3
090122	10:03:04.670	254311386.670	0.429	7	3
090122	12:00:48.740	254318450.740	0.565	7	2
090122	15:35:53.655	254331355.655	0.208	6	2
090122	23:14:54.053	254358896.053	0.520	17	6
090123	01:19:42.448	254366383.448	0.144	9	3
090123	02:42:10.695	254371330.695	0.592	18	5
090123	16:54:38.064	254422479.064	0.220	7	3
090125	23:00:36.087	254617238.087	0.980	10	2
090203	20:00:39.494	255384041.494	0.272	17	6
090204	20:27:20.796	255472042.796	0.236	6	2
090322	22:39:15.786	259454357.786	0.592	10	3
090401	15:59:36.826	260294378.826	0.208	5	2

[a] Mission Elapsed Time, the number of seconds since January 1, 2001

[b] Duration of the Bayesian block.

3. RESULTS

After analyzing 562 overlapping time-segment spectra with three different models and evaluating their BIC values, we found that 506 spectra (equivalent to 90.1% of the sample) were most effectively modeled using the COMPT model. This means that for these spectra, the COMPT model either had the most favorable ΔBIC value or its BIC values were comparable (ΔBIC difference < 10) to those of the other models. The remaining two models, BB+BB and MBB−RCS, were less favored and showed similar performance; the BB+BB model was preferred for 57.5% of the 562 spectra, while the MBB−RCS model was preferred by 58.4% of them.

In the second step of the analysis, we obtained 148 non-overlapping time segments. Among these time segments; $\sim 95\%$, $\sim 54\%$, and $\sim 56\%$ of them can be modeled with the COMPT model, the BB+BB model, and MBB−RCS model respectively. Therefore, in the second round of fitting, we noticed that there is a slight increase in the number of favorable time segments COMPT model, and a slight decrease for the other two models.

3.1 COMPT Model Results

We found that the photon index (Γ) parameter of the COMPT model shows a Gaussian distribution in a range of between –2 and 1. The mean value of this distribution is -0.53 ± 0.05 with a width of 0.47 ± 0.05. This fit corresponds to a reduced chi-square of (χ^2_ν) 0.79. In addition, the $E_{\rm peak}$ parameter of the model is also Gaussian distributed with a mean and width of 31.1 ± 1.9 keV and 10.5 ± 2.4 keV respectively ($\chi^2_\nu = 1.89$). The energy flux of this model fit in the 8−200 keV band ranges from 1.1×10^{-6} to 9.8×10^{-5} erg cm^{-2} s^{-1}. Hence, energy fluence values are between 1.9×10^{-7} and 1.6×10^{-6} erg cm^{-2}.

It is also worth mentioning that there are three outliers in the E_{peak} domain. They have a peak energy of over 50 keV; exactly 55.7, 55.9, and 57.8 keV respectively. These outliers coming from three different bursts and power law indices are not extraordinary; -0.53, -0.96, and -1.04, respectively. Additionally, two of the three outliers are obtained from two spectra with the flux of about 4×10^{-6} erg cm^{-2} s^{-1} and one from a spectrum at the flux of 2×10^{-5} erg cm^{-2} s^{-1}, an order of magnitude lower.

There is not any correlation between parameters of the COMPT model, Spearman's rank order correlation coefficient is (ρ) 0.21, and the chance probability of such correlation to occur from a random data set (P) is 0.0105. On the contrary, there is a positive correlation between the Γ and the corresponding flux with a ρ of 0.56 and P of 2.7×10^{-13}. We also observe that the spectra exhibiting the highest flux levels produce photon indices around 0.5, with their E_{peak} values tending to cluster near 40 keV. Conversely, for spectra at lower flux levels, the E_{peak} values display a broader distribution, spanning a range from approximately 15 keV to 45 keV.

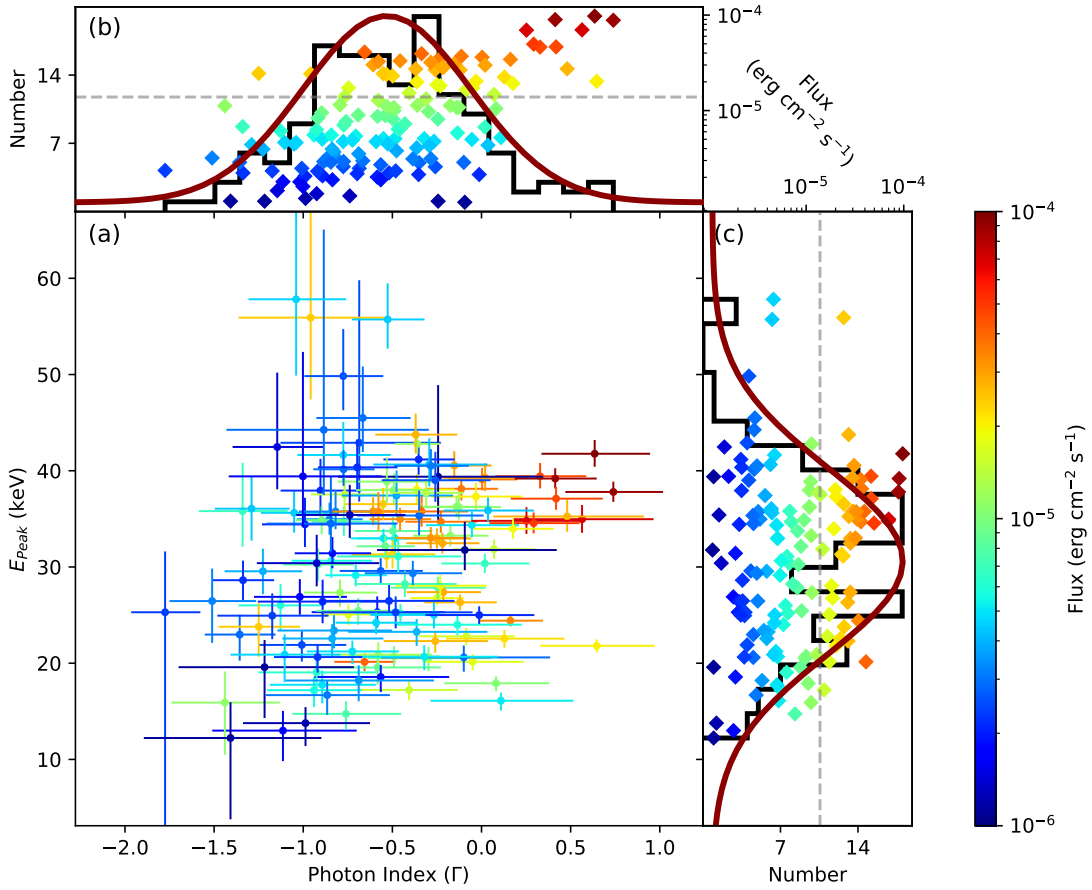

Figure 3.1 (a) The scatter plot of $E_{\rm peak}$ vs. photon index of the COMPT model fits for 141 spectra. Corresponding energy flux values are color-coded. (b) The distribution of Photon Index values, the best-fit Gaussian function model shown in brown, and corresponding flux values are shown as diamond data points. The gray dashed line shows the mean value of fluxes. (c) The distribution of $E_{\rm peak}$, the best-fit Gaussian function model shown in brown, and corresponding flux values are shown as diamond data points. The gray dashed line shows the mean value of fluxes.

3.2 Thermal Models Results

3.2.1 BB+BB Model

As for the BB+BB model results, we observed that the cooler component of the BB+BB model (kT_l) has a Gaussian distribution with a peak at 4.37± 0.16 keV

and a width of 1.0 ± 0.2 ($\chi^2_\nu = 0.82$). This parameter has a narrower spread from 2 to 7 keV. On the other hand, the hotter component of the same model (kT_h) has a much broader distribution, ranging between 6 and 20 keV, yet the shape of the curve is Gaussian. The distribution has a peak at 12 ± 0.49 keV and a width of 3.43 ± 0.55 ($\chi^2_\nu = 1.15$). Nevertheless, kT_l and kT_h parameters are correlated positively ($\rho = 0.84$ and $P = 1.6 \times 10^{-22}$). but they are not correlated with the flux values.

For time segments with larger flux values, we observe that the spectra generally exhibit higher kT_l values. In the case of time segments with intermediate flux values, the kT_l values are predominantly found between 3 and 6 keV. Regarding the flux-dependent behavior of kT_h, its values span almost the entire range from 7.5 keV to approximately 20 keV across all flux levels. The only exception is observed in the highest flux time segments, where the kT_h values are concentrated in a narrower range, specifically between 10 and 11 keV.

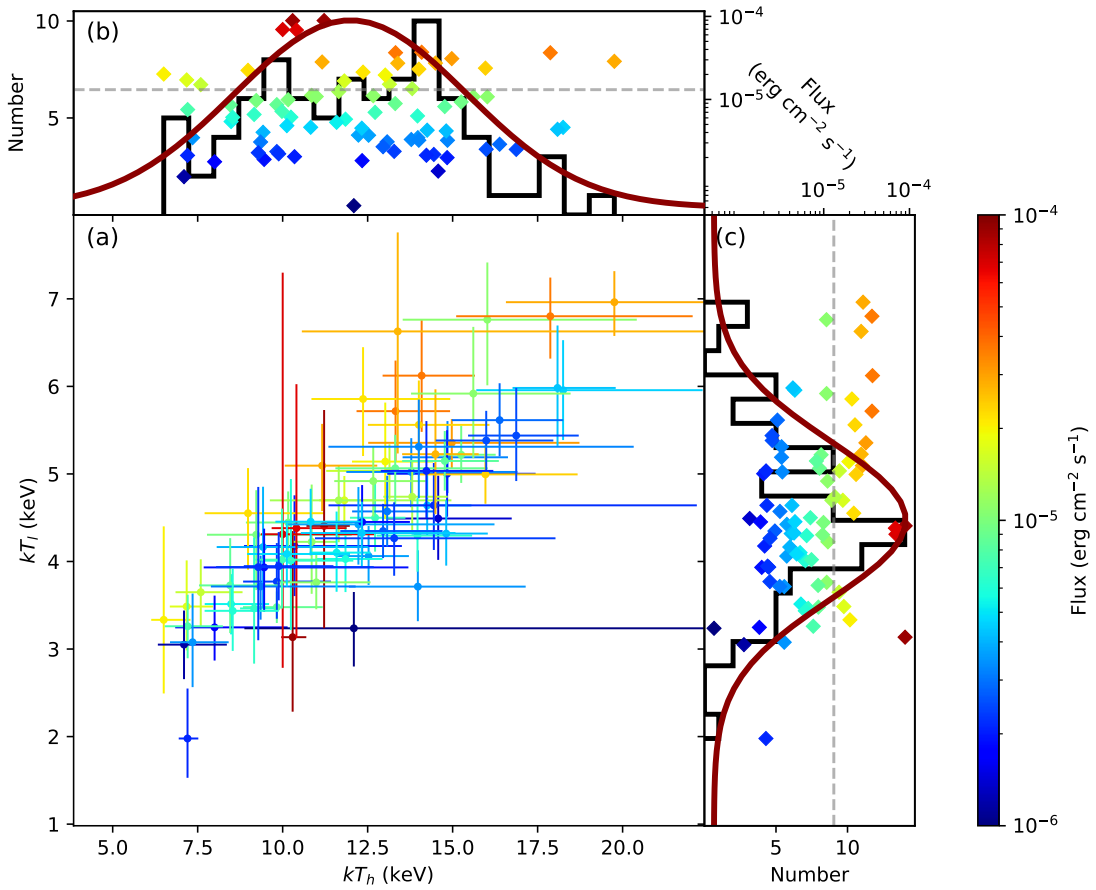

Figure 3.2 (a) The scatter plot of kT_l vs kT_h parameters that can be described with BB+BB (80 spectra). Corresponding flux values are color-coded. (b) The distribution of kT_h, the best-fit Gaussian function model shown in red, and corresponding flux values are shown as diamond data points. The gray dashed line shows the mean value of fluxes. (c) The distribution of kT_l values, the best-fit Gaussian function model shown in red, and corresponding flux values are shown as diamond data points. The gray dashed line shows the mean value of fluxes.

3.2.2 MBB–RCS Model

The distribution of the thermal parameter of MBB−RCS model (kT_m) is between kT_l and kT_h. Its range is in between 4 and 12 keV. Despite the lower number of samples, the distribution of kT_m is consistent with a bimodal distribution beside the single Gaussian distribution. A single Gaussian fit to the distribution peaks at 8.35 ± 0.74 keV and its width is 2.91 ± 1.0 (χ^2_ν = 1.45). Additionally, the addition of two Gaussian functions has the first peak at 5.63 ± 0.45 keV and the second peak at 9.0±0.13 keV. The widths are 1.6 ± 0.3 and 0.88 ± 0.12, respectively (χ^2_ν = 0.47).

In terms of the flux dependence within the MBB−RCS model, the lower and middle flux values exhibit a distribution across the entire range of kT_m values. However, a notable trend is observed with the highest flux values: they tend to cluster around the 8-10 keV region. This clustering interestingly coincides with the second peak of the distribution.

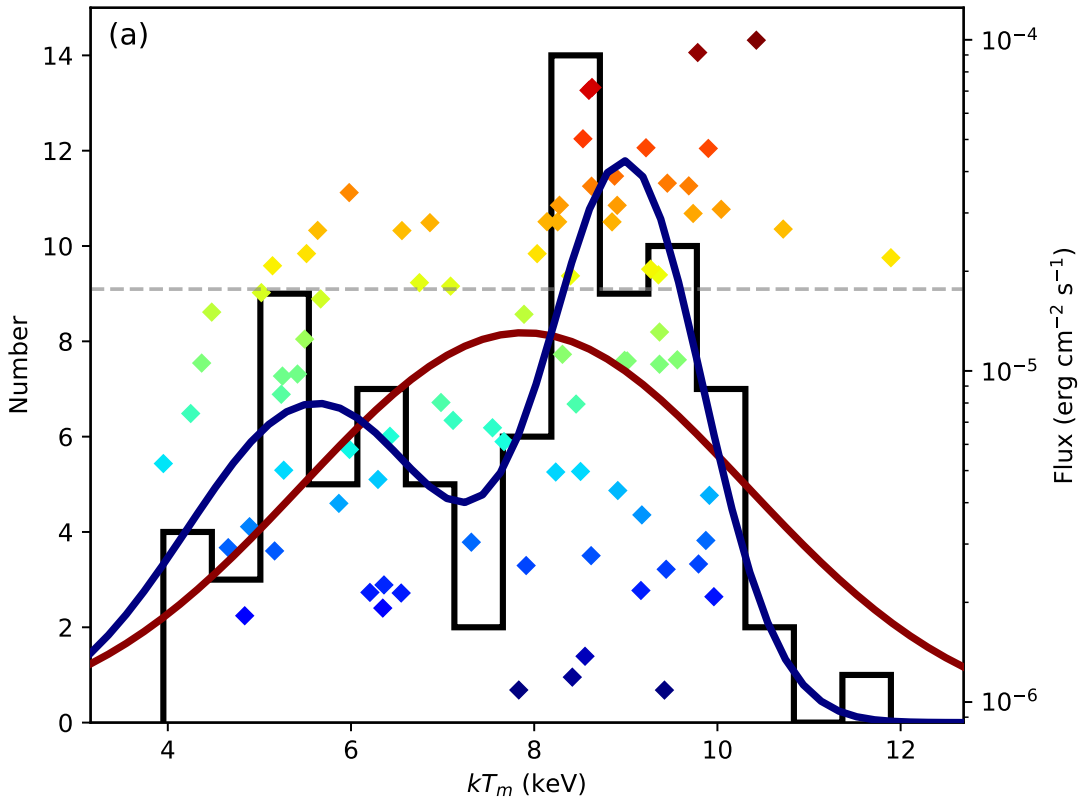

Figure 3.3 Time segment distribution of the MBB-RCS model temperature, kT_m for 83 spectra. Flux values of each individual time segment are shown in logarithmic scale and color-coded diamond data points. The best single Gaussian fit is drawn in red and the best double Gaussian fit is drawn in blue. The gray dashed line shows the mean value of fluxes.

4. DISCUSSION

In this study, we introduced a novel method to examine the time-resolved spectral characteristics of bursts from SGR J1550−5418 . This approach differs significantly from traditional time-resolved spectral analysis methods (see e.g., Younes et al., 2014). Our innovative two-step process employs a clustering algorithm to identify time intervals during bursts that show substantial spectral variations. Consequently, the spectral parameters derived from our method more accurately reflect the source's true spectral behavior, independent of our selection of time bins. Furthermore, our systematic analysis of the time-resolved spectra of SGR J1550−5418 bursts involved the use of a physically-motivated model (MBB-RCS), in addition to the application of standard continuum models (COMPT and BB+BB).

4.1 Comparison to Previous Studies

The burst spectra of SGR J1550−5418 have been examined in previous studies using both time-integrated and time-resolved approaches. Specifically, Younes et al. (2014) and van der Horst et al. (2012) conducted studies on a list of bursts similar to the one we have analyzed.

Younes et al. (2014) studied time-resolved analyses of 63 bursts originating from SGR J1550−5418. Among these bursts, there are 44 bursts in common with ours. Therefore, it is possible to make a valid comparison of the results of the two studies. In the analysis, they employed the COMPT model as one of their continuum models. They reported a Gaussian distribution for the photon index, peaking at -0.55 ± 0.58. This finding is compatible with our result.

Moreover, they graphed $E_{\rm peak}$ vs. Flux and Photon Index vs. Flux plots, resulting in a broken power-law relation in both two plots. For the $E_{\rm peak}$ plot, they found a

low-flux power law index of -0.18 ± 0.02 and a high-flux power law index of 0.12 ± 0.02, with a breakpoint flux at (9.1±0.7)×10^{-6} erg cm^{-2} s^{-1}, corresponding to $E_{\rm peak} = 32 \pm 2$ keV. In comparison, we observed a broken power-law trend in the $E_{\rm peak}$ vs. Flux plot as well. Our results show similar characteristics in higher flux levels with a power-law index of 0.16 ± 0.04. However, this similarity does not extend to lower flux values. In our results, we do not observe any correlation at low flux levels.

About the photon index vs. flux plot, they indicated no correlation up to the breakpoint of $\sim 10^{-5}$ erg cm^{-2} s^{-1}, followed by a similar positive correlation as $E_{\rm peak}$ vs. flux plot. However, our study revealed a double positive power law characterized by slopes of 0.48 ± 0.07 and 1.85 ± 0.40.

In addition, Younes et al. (2014) analyzed the correlation between the blackbody temperature (kT) and the surface area of the inferred emission region (R^2) in four flux regimes. They found that R^2 vs. kT values show broken power-law characteristics above a flux threshold of 3.2×10^{-6} erg cm^{-2} s^{-1}. Below this threshold, the trend aligns with a simple power law. In contrast, our results suggest that the broken power-law model is only valid for the trend at the highest flux levels of F > 3.2×10^{-5} erg cm^{-2} s^{-1}. Below this level, a simple power-law model is enough for describing R^2 vs. kT trends in all lower flux regimes.

It is also worth mentioning another difference between the two studies. Younes et al. (2014) found a broken power law correlation with indexes of 0.2 ± 0.1 and 0.7 ± 0.2 between kT_l and kT_h, while we found a power law correlation which is explained in the previous section.

Regarding the MBB−RCS model, we investigated the R^2 vs. kT behavior with the same flux levels. It was sufficient to represent all four correlations with the power-law model. Our findings indicate that in the two lowest flux regimes, the observed trends align with the predictions of the Stefan-Boltzmann law, where $R^2 \propto kT^4$. However, this pattern begins to diverge from the Stefan-Boltzmann law as the flux increases, and the deviation becomes significant (nearly 7σ) in the highest flux interval.

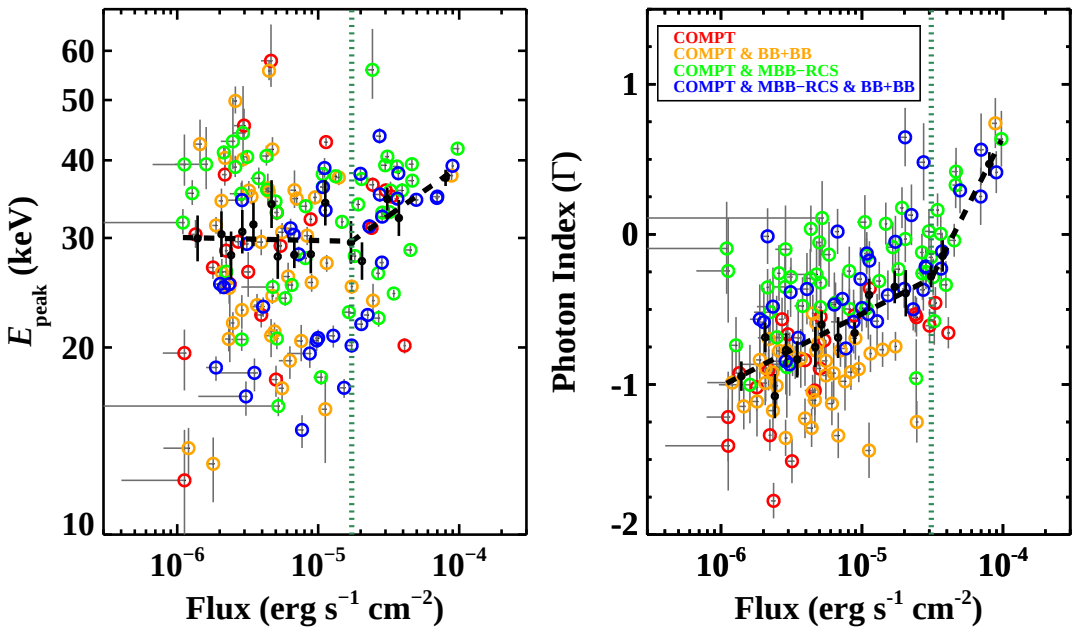

Figure 4.1 The scatter plot of $E_{\rm peak}$ vs. flux (left panel) and photon index vs. flux (right panel). Color code shows the preferred photon model(s) based on BIC values. The black dots represent the weighted means of consecutive groups, each with 10 data points. The black dashed lines show the best fit to the relation between the weighted means of $E_{\rm peak}$ and flux, and between the weighted means of photon index and flux, respectively. The vertical dotted lines in both panels show the flux breaks, which are consistent with each other within their errors.

Table 4.1 Area vs. kT fit parameters for various flux ranges of MBB-RCS and BB+BB models as shown in Figure 5

	MBB-RCS	**BB+BB**		
Flux Range (erg cm^{-2} s^{-1})	α-kT_m	α-kT_l	α-kT_h	kT_{break} (keV)
$F > 10^{-4.5}$	-3.18 ± 0.12	-1.48 ± 0.40	-8.98 ± 0.99	10.81 ± 1.03
$10^{-5.0} < F < 10^{-4.5}$	-3.71 ± 0.06	-4.11 ± 0.11^a	$--$	$--$
$10^{-5.5} < F < 10^{-5.0}$	-4.35 ± 0.08	-3.88 ± 0.08^a	$--$	$--$
$F < 10^{-5.5}$	-4.11 ± 0.10	-3.74 ± 0.11^a	$--$	$--$

^{a} A single PL fit to the data.

van der Horst et al. (2012) revealed an intriguing relationship between flux and the $E_{\rm peak}$: They observed an anti-correlation between these parameters with a power law index of -0.22 up to about 30 keV in $E_{\rm peak}$, equivalent to a flux of 4×10^{-6} erg cm^{-2} s^{-1}, beyond which they become positively correlated with an index of 0.07. In contrast, our results do not show any correlation at low flux levels but do show a positive correlation between flux and $E_{\rm peak}$ with a power law index of 0.16±0.04. This shift in trend happens at a flux of approximately 1.74×10^{-5} erg cm^{-2} s^{-1}.

Despite van der Horst et al. (2012) finding no correlation between the photon index and flux, we found a broken power-law relationship between them with the slope of 0.48±0.07 and 1.85±0.40. The change in this trend, which coincides with the change of trend in the flux−$E_{\rm peak}$ behavior, occurs around a flux of 3.09×10^{-5} erg cm^{-2} s^{-1}.

Additionally, we analyzed the distribution of spectra in the $E_{\rm peak}$ vs. flux and photon index vs. flux planes, categorizing them based on their preferred model. Notably, COMPT is the favored model for all these spectra. We observed that spectra with a preference for the MBB−RCS model, in addition to COMPT, correspond to higher Γ parameters than those favoring the BB+BB and COMPT models, even though both groups are present across all flux levels.

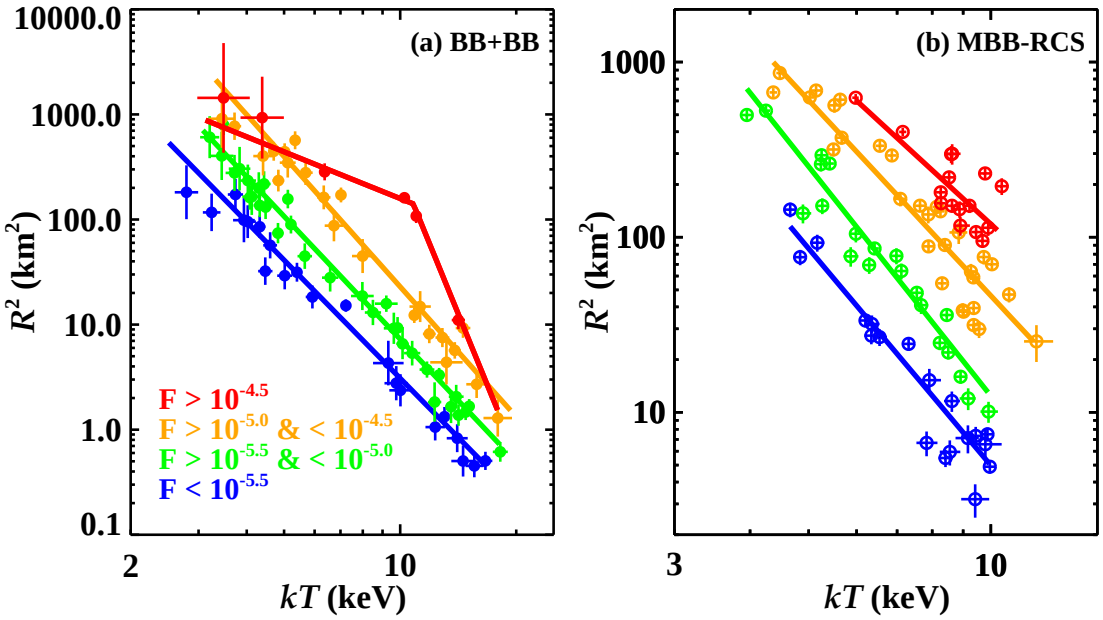

Figure 4.2 [Left] Flux color-coded plot of R^2 vs. kT for BB+BB. Each data point represents the weighted means of R^2 and kT of 2 time segments only for display purposes. Solid lines show the best-fit models. [Right] Flux color-coded scatter plot of R^2 vs. kT for MBB-RCS. Solid lines represent PL fits. Distance = 5 kpc

4.2 Comparison with SGR J1935+2154

We compared the results of SGR J1550−5418 and SGR J1935+2154 (Keskin et al. (in preparation)) in addition to previous studies. We found significant differences in the flux relationships of both parameters from the COMPT model. We observed a positive correlation between flux and Photon Index in SGR J1550−5418 , in particular time segments with the highest fluxes. Despite time segments of SGR J1935+2154 with the highest fluxes also exhibiting Photon Index values around 0 and 0.5, these points represent the median of the distribution, unlike in SGR J1550−5418. Moreover, in SGR J1935−2154, there is a positive correlation between $E_{\rm peak}$ values and flux, with the highest $E_{\rm peak}$ values correlating with the highest flux values. Yet, the flux peaks around the middle of the SGR J1550−5418 distribution. Additionally, in both bursts, $E_{\rm peak}$ and flux values demonstrate a relationship characterized by a broken power-law.

About the BB+BB model analysis, we found a positive correlation between kT_l and kT_h in both two bursts. Also, both two kT values and flux show a positive correlation in SGR J1935−2154, which is not the case in SGR J1550−5418. Instead, the highest flux values are concentrated around the peak of the Gaussian distribution in both two kT values of SGR J1550−5418. Finally, for SGR J1935−2154, the relationship between R^2 and kT values in the BB+BB model can be described using a broken power law, except in the case of the lowest flux group, where both a single and broken power law can fit the data. Conversely, for SGR J1550−5418, the parameters generally exhibit characteristics of a single power law fit, with the only exception being the highest flux group, which displays a broken power law relationship.

MBB−RCS model displays similar flux characteristics in both SGR J1550−5418 and SGR J1935+2154 bursts but they have different distributions. In SGR J1550−5418 , there is a distribution with two peaks, which can be modeled using a double Gaussian, a feature not present in the SGR J1935+2154 distribution. The relations between R^2 and kT_m in both bursts show single power-law fit characteristics across all flux groups. Notably, there is a significant deviation from a Planckian distribution at the highest flux values in SGR J1935−2154. This deviation aligns with expectations, as Yamasaki et al. (2020) described the MBB−RCS model implies that photons emitted from the fireball scatter once by magnetospheric particles in the resonant layer, leading to a tail in the spectrum at higher energies and, consequently, a deviation from a Planckian distribution. In SGR J1550−5418, although there is a deviation at the highest fluxes ($F > 10^{-4.5}$),

it remains relatively close to -4 with $\alpha = -3.18$.

5. CONCLUSIONS AND FUTURE PROSPECTS

In this thesis, we employed a number of machine learning tools to identify significant spectral variations in short magnetar bursts for the first time. We concluded that one of the earliest techniques, namely the K-means clustering is the most robust and effective method in time-resolved spectral analysis of very short transient events. A similar two-stage approach that we incorporated here could be applied to time-resolved spectral investigations of other short transient events, such as, cosmological gamma ray bursts and thermonuclear bursts from neutron stars in low mass X-ray binaries.

The COMPT model is dominantly favored nearly for the whole sample of spectra. However, earlier time-integrated magnetar burst spectral studies showed that the BB+BB model is more preferred (e.g. van der Horst et al., 2012). This is not surprising given the fact that we observe significant variations in $E_{\rm peak}$ throughout the bursts. When these spectra with different $E_{\rm peak}$ values are combined to form the integrated burst spectra, the resulting spectral shape could mimic the form of a BB+BB if $E_{\rm peak}$ values are mostly concentrated around two or more values. Therefore, despite with less statistical significance, the COMPT model yields a better description on short timescales.

The MBB−RCS model is applied systematically for the first time to a large sample of magnetar burst spectra. Even though it is still a toy model (involving only a single scattering) it can explain most ($\sim 60\%$) of the spectral of time segments. We can also see that the R^2 and kT_m relation shows similar characteristics with the Stephan-Boltzmann Law as in Figure [right]. Hence, it lends further support to this relatively simple but physically motivated model for magnetar bursts.

We found a broken power law in R^2 and kT_m relation of BB+BB model only in the flux regime larger than about $3{\times}10^{-5}$ erg cm^{-2} s^{-1} whereas earlier time-resolved spectral investigations showed the deviation from Stephan-Boltzmann Law when flux is higher than $3{\times}10^{-6}$ erg cm^{-2} s^{-1} Younes et al. (2014). This difference could arise from different methodological approaches (number of counts in each spectrum,

arbitrary selection of time segments, etc.). The important fact is that we confirm the presence of a broken power law trend in the R^2 vs kT domain. It was recently suggested that the deviation could be due to anisotropies of the flux tubes that could form in the emission zone.

In the future, different methodologies can be applied to capture spectral change points more precisely. In particular, deep learning methods, such as artificial neural networks can be utilized for this purpose.

In this thesis, we present combined results of our detailed time-resolved spectral analyses. Within this context, we have developed a large set of spectral results for all bursts in our sample. The recent detection of quasi-periodic oscillations (QPOs) in the $E_{\rm peak}$ parameter of an SGR J1935+2154 burst (Roberts et al., 2023) is highly encouraging to systematically search for similar periodic or quasi-periodic variations in the parameters of SGR J1550−5418 bursts.

BIBLIOGRAPHY

Alpar, M. A., Cheng, A. F., Ruderman, M. A., & Shaham, J. (1982). A new class of radio pulsars. , 300(5894), 728–730.

Arnaud, K. A. (1996). XSPEC: The First Ten Years. In Jacoby, G. H. & Barnes, J. (Eds.), Astronomical Data Analysis Software and Systems V, volume 101 of Astronomical Society of the Pacific Conference Series, (pp.17).

Atteia, J. L., Boer, M., Hurley, K., Niel, M., Vedrenne, G., Fenimore, E. E., Klebesadel, R. W., Laros, J. G., Kuznetsov, A. V., Sunyaev, R. A., Terekhov, O. V., Kouveliotou, C., Cline, T., Dennis, B., Desai, U., & Orwig, L. (1987). Localization, Time Histories, and Energy Spectra of a New Type of Recurrent High-Energy Transient Source. , 320, L105.

Baade, W. & Zwicky, F. (1934). Cosmic Rays from Super-novae. Proceedings of the National Academy of Science, 20(5), 259–263.

Backer, D. C., Kulkarni, S. R., Heiles, C., Davis, M. M., & Goss, W. M. (1982). A millisecond pulsar. Nature, 300(5893), 615–618.

Camilo, F., Ransom, S. M., Halpern, J. P., & Reynolds, J. (2007). 1e 1547.0-5408: A radio-emitting magnetar with a rotation period of 2 seconds. The Astrophysical Journal, 666(2).

Cash, W. (1979). Parameter estimation in astronomy through application of the likelihood ratio. , 228, 939–947.

Chadwick, J. (1932). The existence of a neutron. Proc. R. Soc. Lond. A Math. Phys. Sci., 136(830), 692–708.

Chamel, N., Haensel, P., Zdunik, J. L., & Fantina, A. F. (2013). On the Maximum Mass of Neutron Stars. International Journal of Modern Physics E, 22(7), 1330018.

Cocke, W. J., Disney, M. J., & Taylor, D. J. (1969). Discovery of optical signals from pulsar NP 0532. Nature, 221(5180), 525–527.

Collazzi, A. C., Kouveliotou, C., Horst, A. J., Younes, G. A., Kaneko, Y., Göğüş, E., Lin, L., Granot, J., Finger, M. H., Chaplin, V. L., & et al. (2015). The five year fermi/gbm magnetar burst catalog. The Astrophysical Journal Supplement Series, 218(1), 11.

Dib, R. & Kaspi, V. M. (2014). 16 yr of RXTE Monitoring of Five Anomalous X-Ray Pulsars. , 784(1), 37.

Duncan, R. C. & Thompson, C. (1992). Formation of Very Strongly Magnetized Neutron Stars: Implications for Gamma-Ray Bursts. , 392, L9.

Ester, M., Kriegel, H.-P., Sander, J., & Xu, X. (1996). A density-based algorithm for discovering clusters in large spatial databases with noise. In Proceedings of the Second International Conference on Knowledge Discovery and Data Mining, KDD'96, (pp. 226–231). AAAI Press.

Evans, W. D., Klebesadel, R. W., Laros, J. G., Cline, T. L., Desai, U. D., Teegarden, B. J., Pizzichini, G., Hurley, K., Niel, M., & Vedrenne, G. (1980). Location of the gamma-ray transient event of 1979 March 5. , 237, L7–L9.

Feroci, M., Caliandro, G. A., Massaro, E., Mereghetti, S., & Woods, P. M. (2004). Broadband x-ray spectra of short bursts from sgr 1900+14. The Astrophysical Journal, 612(1), 408–413.

Gamow, G. & Schoenberg, M. (1941). Neutrino Theory of Stellar Collapse. Physical Review, 59(7), 539–547.

Gavriil, F. P., Kaspi, V. M., & Woods, P. M. (2002). Magnetar-like X-ray bursts from an anomalous X-ray pulsar. , 419(6903), 142–144.

Giacconi, R., Gursky, H., Kellogg, E., Schreier, E., & Tananbaum, H. (1971). Discovery of Periodic X-Ray Pulsations in Centaurus X-3 from UHURU. , 167, L67.

Göğüş, E., Kouveliotou, C., Woods, P. M., Thompson, C., Duncan, R. C., & Briggs, M. S. (2001). Temporal and Spectral Characteristics of Short Bursts from the Soft Gamma Repeaters 1806-20 and 1900+14. , 558(1), 228–236.

Göğüş, E., Woods, P. M., Kouveliotou, C., Finger, M. H., Pal'shin, V., Kaneko, Y., Golenetskii, S., Frederiks, D., & Airhart, C. (2011). Extended Tails from SGR 1806-20 Bursts. , 740(2), 55.

Gregory, P. C. & Fahlman, G. G. (1980). An extraordinary new celestial x-ray source. Nature, 287(5785), 805–806.

Gruber, D., Goldstein, A., von Ahlefeld, V. W., Bhat, P. N., Bissaldi, E., Briggs, M. S., Byrne, D., Cleveland, W. H., Connaughton, V., Diehl, R., Fishman, G. J., Fitzpatrick, G., Foley, S., Gibby, M., Giles, M. M., Greiner, J., Guiriec, S., van der Horst, A. J., von Kienlin, A., Kouveliotou, C., Layden, E., Lin, L., Meegan, C. A., McGlynn, S., Paciesas, W. S., Pelassa, V., Preece, R. D., Rau, A., Wilson-Hodge, C. A., Xiong, S., Younes, G., & Yu, H.-F. (2014). The fermi gbm gamma-ray burst spectral catalog: Four years of data. Astrophys. J. Suppl. Ser., 211(1), 12.

Haensel, P. (1995). URCA Processes in Dense Matter and Neutron Star Cooling. , 74(3-4), 427–436.

Haensel, P. & Schaeffer, R. (1992). Bulk viscosity of hot-neutron-star matter from direct urca processes. Phys. Rev. D, 45, 4708–4712.

Hewish, A., Bell, S. J., Pilkington, J. D. H., Scott, P. F., & Collins, R. A. (1968). Observation of a Rapidly Pulsating Radio Source. , 217(5130), 709–713.

Hewish, A. & Okoye, S. E. (1965). Evidence for an Unusual Source of High Radio Brightness Temperature in the Crab Nebula. , 207(4992), 59–60.

Hulse, R. A. & Taylor, J. H. (1975). Discovery of a pulsar in a binary system. , 195, L51–L53.

Hurley, K., Boggs, S. E., Smith, D. M., Duncan, R. C., Lin, R., Zoglauer, A., Krucker, S., Hurford, G., Hudson, H., Wigger, C., Hajdas, W., Thompson, C., Mitrofanov, I., Sanin, A., Boynton, W., Fellows, C., von Kienlin, A., Lichti, G., Rau, A., & Cline, T. (2005). An exceptionally bright flare from SGR 1806-20 and the origins of short-duration gamma-ray bursts. Nature, 434(7037), 1098–1103.

Hurley, K., Cline, T., Mazets, E., Barthelmy, S., Butterworth, P., Marshall, F., Palmer, D., Aptekar, R., Golenetskii, S., Il'Inskii, V., Frederiks, D., McTiernan, J., Gold, R., & Trombka, J. (1999). A giant periodic flare from the soft γ-ray repeater SGR1900+14. , 397(6714), 41–43.

Igoshev, A. P., Popov, S. B., & Hollerbach, R. (2021). Evolution of neutron star magnetic fields.

Israel, G. L., Romano, P., Mangano, V., Dall'Osso, S., Chincarini, G., Stella, L., Campana, S., Belloni, T., Tagliaferri, G., Blustin, A. J., & et al. (2008). A swift gaze into the 2006 march 29 burst forest of sgr 1900+14. The Astrophysical

Journal, 685(2), 1114–1128.
Kaspi, V. M. & Beloborodov, A. M. (2017). Magnetars. Annual Review of Astronomy and Astrophysics, 55(1), 261–301.
Kass, R. E. & Raftery, A. E. (1995). Bayes factors. Journal of the American Statistical Association, 90(430), 773–795.
Kniffen, D. A., Hartman, R. C., Thompson, D. J., Bignami, G. F., & Fichtel, C. E. (1974). Gamma radiation from the Crab Nebula above 35 MeV. , 251(5474), 397–399.
Kouveliotou, C., Dieters, S., Strohmayer, T., van Paradijs, J., Fishman, G. J., Meegan, C. A., Hurley, K., Kommers, J., Smith, I., Frail, D., & Murakami, T. (1998). An X-ray pulsar with a superstrong magnetic field in the soft γ-ray repeater SGR1806 - 20. , 393(6682), 235–237.
Kırmızıbayrak, D., Şaşmaz Muş, S., Kaneko, Y., & Göğüş, E. (2017). Broad-band spectral investigations of magnetar bursts. The Astrophysical Journal Supplement Series, 232(1), 17.
Lamb, R. C. & Markert, T. H. (1981). X-ray emission from supernova remnants near gamma-ray sources. The Astrophysical Journal, 244, 94.
Lander, S. K. (2021). Generating neutron-star magnetic fields: three dynamo phases. , 507(1), L36–L40.
Laros, J. G., Fenimore, E. E., Klebesadel, R. W., Atteia, J.-L., Boer, M., Hurley, K., Niel, M., Vedrenne, G., Kane, S. R., Kouveliotou, C., Cline, T. L., Dennis, B. R., Desai, U. D., Orwig, L. E., Kuznetsov, A. V., Sunyaev, R. A., & Terekhov, O. V. (1987). A new type of repetitive behavior in a high-energy transient. Astrophys. J., 320, L111.
Liddle, A. R. (2007). Information criteria for astrophysical model selection. , 377(1), L74–L78.
Lin, L., Göğüş, E., Baring, M. G., Granot, J., Kouveliotou, C., Kaneko, Y., van der Horst, A., Gruber, D., von Kienlin, A., Younes, G., Watts, A. L., & Gehrels, N. (2012). Broadband Spectral Investigations of SGR J1550-5418 Bursts. , 756(1), 54.
Lloyd, S. (1982). Least squares quantization in PCM. IEEE Trans. Inf. Theory, 28(2), 129–137.
Lyubarsky, Y. E. (2002). On the x-ray spectra of soft gamma repeaters. Monthly Notices of the Royal Astronomical Society, 332(1), 199–204.
Mazets, E. P., Golenetskii, S. V., Il'inskii, V. N., Aptekar', R. L., & Guryan, Y. A. (1979). Observations of a flaring x-ray pulsar in dorado. Nature, 282(5739), 587–589.
Meegan, C., Lichti, G., Bhat, P. N., Bissaldi, E., Briggs, M. S., Connaughton, V., Diehl, R., Fishman, G., Greiner, J., Hoover, A. S., van der Horst, A. J., von Kienlin, A., Kippen, R. M., Kouveliotou, C., McBreen, S., Paciesas, W. S., Preece, R., Steinle, H., Wallace, M. S., Wilson, R. B., & Wilson-Hodge, C. (2009). THE FERMI GAMMA-RAY BURST MONITOR. Astrophys. J., 702(1), 791–804.
Muş, S. Ş., , S., Göğüş, E., Kaneko, Y., Chakraborty, M., & Aydın, B. (2015). Burst Tails from SGR J1550-5418 Observed with the Rossi X-Ray Timing Explorer. , 807(1), 42.
Olausen, S. A. & Kaspi, V. M. (2014). The McGill Magnetar Catalog. , 212(1), 6.
Pedregosa, F., Varoquaux, G., Gramfort, A., Michel, V., Thirion, B., Grisel, O.,

Blondel, M., Prettenhofer, P., Weiss, R., Dubourg, V., Vanderplas, J., Passos, A., Cournapeau, D., Brucher, M., Perrot, M., & Édouard Duchesnay (2011). Scikit-learn: Machine learning in python. Journal of Machine Learning Research, 12(85), 2825–2830.

Rea, N. & Esposito, P. (2011). Magnetar outbursts: an observational review. In High-Energy Emission from Pulsars and their Systems, volume 21 of Astrophysics and Space Science Proceedings, (pp. 247).

Roberts, O. J., Baring, M. G., Huppenkothen, D., Kouveliotou, C., Göğüş, E., Kaneko, Y., Lin, L., van der Horst, A. J., & Younes, G. (2023). Quasiperiodic Peak Energy Oscillations in X-Ray Bursts from SGR J1935+2154. , 956(1), L27.

Romani, R. W., Kandel, D., Filippenko, A. V., Brink, T. G., & Zheng, W. (2022). Psr j09520607: The fastest and heaviest known galactic neutron star. The Astrophysical Journal Letters, 934(2), L17.

Suwa, Y., Yoshida, T., Shibata, M., Umeda, H., & Takahashi, K. (2018). On the minimum mass of neutron stars. Monthly Notices of the Royal Astronomical Society, 481(3), 3305–3312.

van der Horst, A. J., Kouveliotou, C., Gorgone, N. M., Kaneko, Y., Baring, M. G., Guiriec, S., Göğüş, E., Granot, J., Watts, A. L., Lin, L., Bhat, P. N., Bissaldi, E., Chaplin, V. L., Finger, M. H., Gehrels, N., Gibby, M. H., Giles, M. M., Goldstein, A., Gruber, D., Harding, A. K., Kaper, L., von Kienlin, A., van der Klis, M., McBreen, S., Mcenery, J., Meegan, C. A., Paciesas, W. S., Pe'er, A., Preece, R. D., Ramirez-Ruiz, E., Rau, A., Wachter, S., Wilson-Hodge, C., Woods, P. M., & Wijers, R. A. M. J. (2012). SGR J1550-5418 Bursts Detected with the Fermi Gamma-Ray Burst Monitor during its Most Prolific Activity. , 749(2), 122.

van Paradijs, J., Taam, R. E., & van den Heuvel, E. P. J. (1995). On the nature of the 'anomalous' 6-s X-ray pulsars. , 299, L41.

von Kienlin, A., Gruber, D., Kouveliotou, C., Granot, J., Baring, M. G., Göğüş, E., Huppenkothen, D., Kaneko, Y., Lin, L., Watts, A. L., Bhat, N. P., Guiriec, S., van der Horst, A. J., Bissaldi, E., Greiner, J., Meegan, C. A., Paciesas, W. S., Preece, R. D., & Rau, A. (2012). Detection of Spectral Evolution in the Bursts Emitted during the 2008-2009 Active Episode of SGR J1550-5418. , 755(2), 150.

Woods, P. M., Kaspi, V. M., Thompson, C., Gavriil, F. P., Marshall, H. L., Chakrabarty, D., Flanagan, K., Heyl, J., & Hernquist, L. (2004). Changes in the X-Ray Emission from the Magnetar Candidate 1E 2259+586 during Its 2002 Outburst. , 605(1), 378–399.

Woosley, S. E., Heger, A., & Weaver, T. A. (2002). The evolution and explosion of massive stars. Reviews of Modern Physics, 74(4), 1015–1071.

Yamasaki, S., Lyubarsky, Y., Granot, J., & Göğüş, E. (2020). Spectral modification of magnetar flares by resonant cyclotron scattering. , 498(1), 484–494.

Younes, G., Kouveliotou, C., van der Horst, A. J., Baring, M. G., Granot, J., Watts, A. L., Bhat, P. N., Collazzi, A., Gehrels, N., Gorgone, N., Göğüş, E., Gruber, D., Grunblatt, S., Huppenkothen, D., Kaneko, Y., von Kienlin, A., van der Klis, M., Lin, L., Mcenery, J., van Putten, T., & Wijers, R. A. M. J. (2014). Time Resolved Spectroscopy of SGR J1550-5418 Bursts Detected with Fermi/Gamma-Ray Burst Monitor. , 785(1), 52.